

# SN 2015U: A Rapidly Evolving and Luminous Type Ibn Supernova

Isaac Shivvers,<sup>1\*</sup> WeiKang Zheng,<sup>1</sup> Jon Mauerhan,<sup>1</sup> Io K. W. Kleiser,<sup>1,2</sup>  
 Schuyler D. Van Dyk,<sup>3</sup> Jeffrey M. Silverman,<sup>4</sup> Melissa L. Graham,<sup>1</sup>  
 Patrick L. Kelly,<sup>1</sup> Alexei V. Filippenko,<sup>1</sup> Sahana Kumar<sup>1</sup>

<sup>1</sup>*Department of Astronomy, University of California, Berkeley, CA 94720-3411, USA*

<sup>2</sup>*Department of Astronomy, California Institute of Technology, Pasadena, CA 91125, USA*

<sup>3</sup>*IPAC/Caltech, Mail Code 100-22, Pasadena, CA 91125, USA*

<sup>4</sup>*Department of Astronomy, University of Texas, Austin, TX 78712, USA*

Submitted to MNRAS

## ABSTRACT

Supernova (SN) 2015U (also known as PSN J07285387+3349106) was discovered in NGC 2388 on 2015 Feb. 11. A rapidly evolving and luminous event, it showed effectively hydrogen-free spectra dominated by relatively narrow helium P-Cygni spectral features and it was classified as a SN Ibn. In this paper we present photometric, spectroscopic, and spectropolarimetric observations of SN 2015U, including a Keck/DEIMOS spectrum (resolution  $\approx 5000$ ) which fully resolves the optical emission and absorption features. We find that SN 2015U is best understood via models of shock breakout from extended and dense circumstellar material (CSM), likely created by a history of mass loss from the progenitor with an extreme outburst within  $\sim 1$ – $2$  yr of core collapse (but we do not detect any outburst in our archival imaging of NGC 2388). We argue that the high luminosity of SN 2015U was powered not through  $^{56}\text{Ni}$  decay but via the deposition of kinetic energy into the ejecta/CSM shock interface. Though our analysis is hampered by strong host-galaxy dust obscuration (which likely exhibits multiple components), our dataset makes SN 2015U one of the best-studied Type Ibn supernovae and provides a bridge of understanding to other rapidly fading transients, both luminous and relatively faint.

**Key words:** supernovae: individual: SN 2015U – stars: mass loss

## 1 INTRODUCTION

Core-collapse supernovae (SNe) are luminous explosions that mark the end of a massive star’s life. These SNe are differentiated from their thermonuclear counterparts (Type Ia SNe) and are grouped into classes via spectral and photometric analyses (e.g., Filippenko 1997). The major core-collapse subclasses include SNe IIP and IIL, events which show strong hydrogen throughout their evolution and respectively do or do not exhibit a hydrogen-recombination plateau in their light curves (though the distinction between SNe IIP and IIL may be less clear than previously thought; e.g., Arcavi et al. 2012; Anderson et al. 2014; Sanders et al. 2015). SNe Ib and Ic (often called stripped-envelope SNe) are core-collapse events that show no hydrogen in their spectra and (for SNe Ic and broad-lined SNe Ic) no helium; they (along with the intermediate SNe IIB, which exhibit very

little hydrogen) are commonly understood to arise from progenitor stars that have lost all or most of their hydrogen (and perhaps helium) envelopes prior to core collapse, though the detailed connections between progenitors and SN observables remain somewhat uncertain (e.g., Matheson et al. 2001; Drout et al. 2011; Bianco et al. 2014; Modjaz et al. 2014; Liu et al. 2015; Dessart et al. 2015).

A subset of SNe reveal signatures of a dense shroud of circumstellar material (CSM) surrounding their progenitors at the time of explosion. For hydrogen-rich events, relatively narrow lines (full width at half-maximum intensity [FWHM]  $\lesssim 1000 \text{ km s}^{-1}$ ) from this interaction with the CSM are often detected; these objects have been dubbed SNe IIn (e.g., Schlegel 1990; Filippenko 1991). This interaction can provide a significant luminosity boost (as has been observed for superluminous SNe IIn; e.g., Gal-Yam 2012). CSM interaction occurs in some hydrogen-poor SNe as well. SNe Ia-CSM are thermonuclear events that exhibit relatively narrow features (usually  $\text{H}\alpha$  emission) caused by interaction

\* E-mail: ishivvers@berkeley.edu

with hydrogen-rich CSM (though the underlying SN ejecta are hydrogen-poor; e.g., Silverman et al. 2013b,a). A small number of stripped-envelope SNe have been found to exhibit the spectral signatures of CSM interaction. SNe Ibn (e.g., Foley et al. 2007; Pastorello et al. 2008a) show relatively narrow helium lines in their spectra but no hydrogen, and they can be quite heterogeneous in their photometric evolution (e.g., Pastorello et al. 2016), while the remarkable SN 2014C appeared to be a normal SN Ib at peak brightness but then began interacting with hydrogen-rich CSM only a few months later (Milisavljevic et al. 2015).

In addition to the examples of interaction with dense CSM described above, indications of very short-lived interaction with CSM have been discovered through “flash spectroscopy” of very young SNe of various types (e.g., Gal-Yam et al. 2014; Shivvers et al. 2015; Khazov et al. 2016). These examples exist on a continuum of CSM densities with the strongly interacting events described above; they require much less CSM and their observables at peak brightness generally align with those of “normal” events.

Here we present the results of our observational campaign to study SN 2015U, a remarkable and very well-monitored SN Ibn. It was discovered in NGC 2388 by the Lick Observatory Supernova Search (LOSS) with the 0.76 m Katzman Automatic Imaging Telescope (KAIT; Filippenko et al. 2001) on 2015 Feb. 11 (all dates and times reported herein are UTC). Note that, because the official International Astronomical Union name was not assigned until November 2015 (Kumar et al. 2015), this event has also been discussed in the literature under the name PSN J07285387+3349106. Ochner et al. (2015) classified it as a young SN Ibn based upon spectra obtained on Feb. 18, which showed a blue continuum and relatively narrow He I emission features (see also Kumar et al. 2015). Tsvetkov et al. (2015) present *BVRI* photometry of SN 2015U starting Feb. 17, showing that it has one of the fastest decline rates known (similar to those of SNe 2002bj, 2005ek, and 2010X) and is remarkably luminous (though SN 2015U is significantly obscured by an uncertain amount of dust in the host galaxy). Pastorello et al. (2015c) present additional photometry and low-resolution spectra of this event and describe SN 2015U within the context of SNe Ibn (e.g., Foley et al. 2007; Pastorello et al. 2008a, 2016).

In this paper we present photometric, spectroscopic, and spectropolarimetric observations of SN 2015U, including one epoch of relatively high-resolution Keck DEIMOS spectroscopy ( $R = \lambda/\delta\lambda \approx 5000$ ), enabling us to study the narrow-line features in detail. We show that SN 2015U is similar to several other SNe from the heterogeneous SN Ibn class, and that it shares many features with the rapid and luminous transients discovered in the Pan-STARRS1 (PS1) archives (Drout et al. 2014), those found in the SuperNova Legacy Survey (SNLS) archives (Arcavi et al. 2016), and a few other rapidly fading SNe from the literature. SN 2015U offers valuable insights into the physics of the poorly observed class of rapidly fading SNe.

## 2 OBSERVATIONS

### 2.1 Photometry

SN 2015U was first detected by KAIT on Feb. 11.24 at  $18.06 \pm 0.15$  mag in an unfiltered image.<sup>1</sup> An unfiltered image taken the night before (Feb. 10.30) shows no source to a limit of  $\sim 18.4$  mag. We began acquiring multiband photometry (*BVRI* and *clear*) starting Feb. 14 with KAIT and the 1 m Nickel telescope at Lick Observatory. We used a set of 50 Nickel and KAIT images with strong detections of SN 2015U and with good astrometric solutions for the field to calculate an updated position:  $\alpha = 07^h28^m53.90^s$ ,  $\delta = +33^\circ49'10.56''$  (J2000), offset from the centre of the galaxy by  $\sim 6''$ . We believe this position to be accurate within  $0.15''$  or better — the positions we measured for the SN exhibit a scatter of  $0.09''$  in both right ascension and declination across 50 images.

Ganeshalingam et al. (2010) describe our photometric observing program at Lick in detail, along with our KAIT and Nickel image-reduction pipeline. Point-spread-function (PSF) photometry was performed using DAOPHOT (Stetson 1987) from the IDL Astronomy User’s Library.<sup>2</sup> Instrumental magnitudes were calibrated to several nearby stars from the Sloan Digital Sky Survey, transformed into the Landolt system using the empirical prescription presented by Robert Lupton.<sup>3</sup>

We measure SN 2015U’s date of peak of brightness in each passband of our Nickel+KAIT photometry by fitting a low-order polynomial to the light curve within the first week (first 10 days for the *I* band) and use Monte Carlo Markov Chain (MCMC) methods to estimate our uncertainties. In Modified Julian Day (MJD), we find  $t_V^{\max} = 57071.1 \pm 0.2$ ,  $t_R^{\max} = 57071.6 \pm 0.5$ , and  $t_I^{\max} = 57072.4 \pm 0.2$  (our data do not constrain the *B*-band peak well). Throughout our analysis we present phases relative to the V-band peak. NGC 2388 is at a redshift of  $z_{\text{host}} = 0.013790 \pm 0.000017$  (NED; de Vaucouleurs et al. 1991), which (assuming cosmological parameters  $H_0 = 71 \text{ km s}^{-1} \text{ Mpc}^{-1}$ ,  $\Omega_m = 0.27$ , and  $\Omega_\Lambda = 0.73$ ) translates into a luminosity distance of 58.9 Mpc (Wright 2006) and a distance modulus of 33.85 mag that we adopt for all absolute-magnitude corrections.

NGC 2388 and the SN site (pre-explosion) were imaged on 2004 Sep. 10 with the *Hubble Space Telescope* (*HST*) and the Near-Infrared Camera and Multi-Object Spectrometer (NICMOS) with the NIC2 aperture (scale  $0''.076 \text{ pixel}^{-1}$ ) in bands *F110W*, *F160W*, *F187N*, and *F190N*. We determined the SN position in each band’s mosaic data products based on the absolute SN position and the world coordinate system of the image — no stellar object was detected at this position in any of the mosaics. We quantified these nondetections in the *F110W* and *F160W* mosaics using DAOPHOT by assuming a PSF constructed from the brightest isolated star in the mosaics and inserting an artificial star at the SN position. The artificial star was measured with ALL-

<sup>1</sup> The KAIT *clear* passband is similar to the *R* band but broader. For more details and transformations to standard passbands, see Riess et al. (1999) and Li et al. (2003).

<sup>2</sup> <http://idlastro.gsfc.nasa.gov/>

<sup>3</sup> <http://www.sdss.org/dr7/algorithms/sdssUBVRITransform.html>

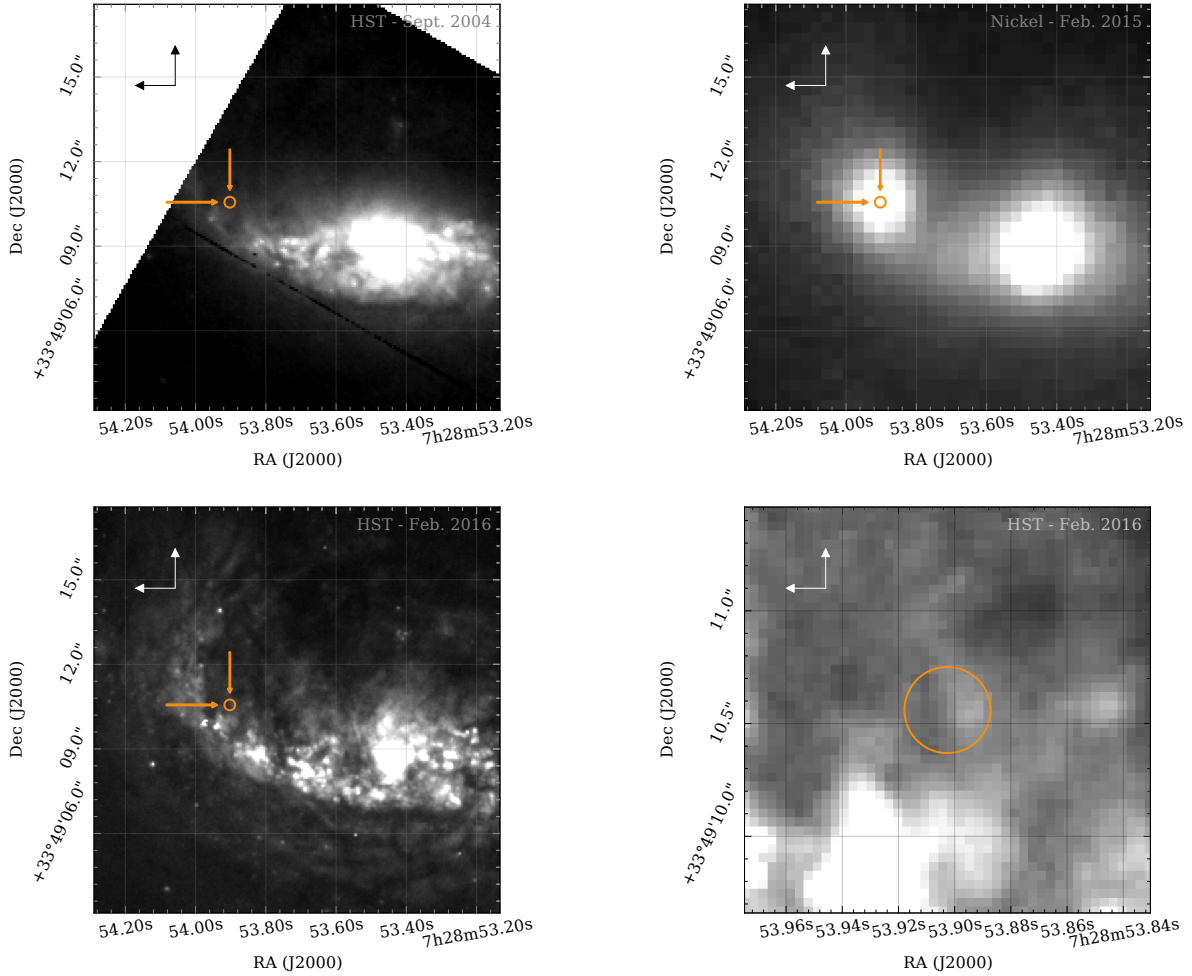


**Figure 1.** Top left: a pre-detection *HST* NICMOS image of NGC 2388 through the *F110W* filter. Top right: a detection of SN 2015U by the Lick Nickel 1 m telescope through the V-band filter. Bottom left: an *HST* WFC3 image of SN 2015U's location through the *F555W* filter at  $\sim 1$  yr post-explosion. Bottom right: a zoom-in of SN 2015U's location in the *HST* *F555W* filter. All images show the location of the SN with orange arrows, and the size of our  $3\sigma$  position error is marked with a circle.

STAR within DAOPHOT using photometric calibrations established from the online cookbook<sup>4</sup> and with parameters appropriate for NIC2, and then reduced in luminosity until it was detected at a signal-to-noise ratio (S/N) of  $\sim 3$ . The corresponding upper limits are  $> 26.0$  and  $> 25.2$  mag in *F110W* and *F160W*, respectively.

Under our Cycle 23 Snapshot program with *HST*'s Wide Field Camera 3 (WFC3; GO-14149, PI Filippenko), we obtained images of the SN location on 2016 Feb. 14 (1 yr post explosion) through the *F555W* (710 s) and *F814W* (780 s) filters (scale  $0''.04$  pixel<sup>-1</sup>). Figure 1 shows a Nickel detection of SN 2015U alongside the pre-explosion NICMOS *F110W* image and the 1 yr WFC3 *F555W* image of the SN location. We find that SN 2015U exploded on the trailing edge of NGC 2388's spiral arm, in a region with several probable dust lanes and a generally clumpy appearance. One of those

clumps falls within the  $3\sigma$  position error circle in both the *F555W* and *F814W* images and is not detected in the pre-explosion NICMOS images. However, this clump appears to be extended and smoothly connected with other bright regions, not point-like, and we therefore attribute it to the host galaxy and not to SN 2015U.

Table 1 presents our photometry of SN 2015U before applying any dust reddening corrections, and Figure 2 shows the light curves after correcting for Milky Way (MW) dust absorption. The data are also available for download from the Berkeley SuperNova DataBase (SNDB; Silverman et al. 2012).<sup>5</sup>

## 2.2 Spectroscopy

We began a spectral monitoring campaign of SN 2015U on 2015 Feb. 15, obtaining six spectra with the Kast double spectrograph (Miller & Stone 1993) on the Shane 3 m

<sup>4</sup> [www.stsci.edu/hst/nicmos/performance/photometry/cookbook.html](http://www.stsci.edu/hst/nicmos/performance/photometry/cookbook.html); corrections to infinite aperture and zero-points at zero magnitude were obtained from [www.stsci.edu/hst/nicmos/performance/photometry/postnics\\_keywords.html](http://www.stsci.edu/hst/nicmos/performance/photometry/postnics_keywords.html).

<sup>5</sup> <http://heracles.astro.berkeley.edu/sndb/>

**Table 1.** KAIT and Nickel Photometry of SN 2015U

| UT Date    | MJD      | <i>B</i> ( $1\sigma$ ) | <i>V</i> ( $1\sigma$ ) | <i>R</i> ( $1\sigma$ ) | <i>I</i> ( $1\sigma$ ) | <i>clear</i> ( $1\sigma$ ) | Instrument |
|------------|----------|------------------------|------------------------|------------------------|------------------------|----------------------------|------------|
| 2015-02-10 | 57063.30 | -                      | -                      | -                      | -                      | >18.4                      | KAIT       |
| 2015-02-11 | 57064.24 | -                      | -                      | -                      | -                      | 18.06 (0.15)               | KAIT       |
| 2015-02-13 | 57066.22 | -                      | -                      | -                      | -                      | 16.85 (0.06)               | KAIT       |
| 2015-02-14 | 57067.35 | 17.71 (0.17)           | 16.98 (0.09)           | 16.46 (0.06)           | 16.18 (0.08)           | 16.57 (0.05)               | KAIT       |
| 2015-02-15 | 57068.22 | 17.65 (0.11)           | 16.86 (0.05)           | 16.41 (0.03)           | 16.23 (0.06)           | -                          | KAIT       |
| 2015-02-17 | 57070.19 | 17.65 (0.09)           | 16.74 (0.04)           | 16.15 (0.05)           | 15.88 (0.05)           | 16.23 (0.03)               | KAIT       |
| 2015-02-18 | 57071.21 | 17.69 (0.08)           | 16.67 (0.04)           | 16.21 (0.03)           | 15.77 (0.04)           | 16.18 (0.03)               | KAIT       |
| 2015-02-19 | 57072.23 | 17.68 (0.09)           | 16.75 (0.04)           | 16.27 (0.03)           | 15.87 (0.04)           | 16.28 (0.03)               | KAIT       |
| 2015-02-20 | 57073.24 | 17.90 (0.13)           | 16.82 (0.04)           | 16.29 (0.03)           | 15.88 (0.04)           | 16.28 (0.02)               | KAIT       |
| 2015-02-21 | 57074.18 | 17.86 (0.10)           | 16.85 (0.05)           | 16.29 (0.04)           | 15.86 (0.04)           | 16.35 (0.02)               | KAIT       |
| 2015-02-22 | 57075.20 | 17.94 (0.09)           | 17.02 (0.04)           | 16.43 (0.03)           | 15.97 (0.04)           | 16.48 (0.02)               | KAIT       |
| 2015-02-22 | 57075.32 | 18.03 (0.02)           | 17.05 (0.01)           | 16.44 (0.01)           | 15.97 (0.01)           | -                          | Nickel     |
| 2015-02-23 | 57076.20 | 18.07 (0.13)           | 17.02 (0.05)           | 16.46 (0.04)           | 16.06 (0.04)           | 16.48 (0.03)               | KAIT       |
| 2015-02-24 | 57077.19 | 18.11 (0.14)           | 17.18 (0.05)           | 16.54 (0.04)           | 16.13 (0.05)           | 16.64 (0.02)               | KAIT       |
| 2015-02-25 | 57078.19 | 18.22 (0.15)           | 17.24 (0.06)           | 16.62 (0.04)           | 16.16 (0.04)           | 16.63 (0.03)               | KAIT       |
| 2015-02-26 | 57079.21 | 18.45 (0.24)           | 17.40 (0.08)           | 16.79 (0.05)           | 16.26 (0.06)           | 16.74 (0.03)               | KAIT       |
| 2015-02-26 | 57079.30 | 18.51 (0.04)           | 17.47 (0.02)           | 16.79 (0.01)           | 16.27 (0.02)           | -                          | Nickel     |
| 2015-02-27 | 57080.21 | 18.53 (0.23)           | 17.44 (0.07)           | 16.89 (0.05)           | 16.41 (0.06)           | 16.91 (0.04)               | KAIT       |
| 2015-03-03 | 57084.23 | -                      | 17.99 (0.27)           | 17.42 (0.13)           | 17.03 (0.16)           | 17.21 (0.10)               | KAIT       |
| 2015-03-03 | 57084.35 | 18.95 (0.11)           | 18.15 (0.05)           | 17.44 (0.03)           | 16.74 (0.02)           | -                          | Nickel     |
| 2015-03-04 | 57085.22 | -                      | 18.01 (0.15)           | 17.63 (0.12)           | 17.24 (0.13)           | 17.56 (0.08)               | KAIT       |
| 2015-03-05 | 57086.19 | -                      | 18.15 (0.22)           | 17.84 (0.16)           | -                      | 17.82 (0.09)               | KAIT       |
| 2015-03-06 | 57087.20 | -                      | 18.73 (0.19)           | 18.15 (0.17)           | 17.70 (0.13)           | -                          | KAIT       |
| 2015-03-06 | 57087.25 | -                      | -                      | -                      | -                      | 17.81 (0.13)               | KAIT       |
| 2015-03-07 | 57088.21 | -                      | 18.62 (0.24)           | 18.26 (0.18)           | 18.14 (0.33)           | -                          | KAIT       |
| 2015-03-08 | 57089.19 | -                      | -                      | 18.62 (0.22)           | -                      | 18.33 (0.17)               | KAIT       |
| 2015-03-08 | 57089.28 | >20.5                  | 19.75 (0.13)           | 18.78 (0.06)           | 17.96 (0.07)           | -                          | Nickel     |
| 2015-03-09 | 57090.17 | -                      | -                      | -                      | -                      | >19.3                      | KAIT       |
| 2015-03-10 | 57091.19 | -                      | -                      | -                      | -                      | >19.6                      | KAIT       |
| 2015-03-12 | 57093.20 | -                      | -                      | -                      | -                      | >19.5                      | KAIT       |
| 2015-03-13 | 57094.17 | -                      | -                      | -                      | -                      | >19.3                      | KAIT       |
| 2015-03-26 | 57107.28 | >21.1                  | >20.9                  | >20.9                  | >20.3                  | -                          | Nickel     |
| 2015-03-30 | 57111.28 | >20.3                  | >20.2                  | >20.3                  | >20.0                  | -                          | Nickel     |

telescope at Lick Observatory and one spectrum with the DEIMOS spectrograph (Faber et al. 2003) on the Keck-II 10 m telescope. Details of our spectral observations are listed in Table 2, and all reductions and calibrations were performed with standard tools and methods, including IRAF routines and custom Python and IDL codes<sup>6</sup> (e.g., Matheson et al. 2000; Pérez & Granger 2007; Silverman et al. 2012).

All spectra were taken at or near the parallactic angle (Filippenko 1982), and the amount of galaxy flux falling into the slit varied as a function of seeing and the slit orientation on the sky. For the spectra which included a large amount of host-galaxy flux (Feb. 18, 21, and 24), we extract a spectrum from a region of the galaxy that does not include any SN 2015U flux, perform a median-filter smoothing to obtain the galaxy continuum, and then subtract it from our spectra, after determining a best-fit galaxy scaling coefficient by comparing synthetic photometry to the multiband photometry observed the same night. We do not attempt to remove the narrow (unresolved) galaxy emission features, so our spectra show varying degrees of narrow-line contamination from the host (including H $\alpha$ , H $\beta$ , and [S II]).

We renormalise each spectrum to match our template-

subtracted *V* or *R*-band photometry (depending on the spectral wavelength coverage) after linearly interpolating the photometry to the time of spectral observation. Figure 3 shows our total-flux spectra of SN 2015U. All spectra are available to download from the Berkeley SNDB and the Weizmann Interactive Supernova Data REPOSITORY (Wiserep; Yaron & Gal-Yam 2012).<sup>7</sup>

Using narrow H $\alpha$  host-galaxy emission in our DEIMOS spectrum, we measure a line-of-sight redshift at the SN's location:  $z_{\text{SN}} = 0.013161 \pm 0.000005$ , a difference of  $\sim 200 \text{ km s}^{-1}$  from the published redshift of the host galaxy — consistent with the SN's position on the approaching arm of this spiral galaxy.

### 2.3 Spectropolarimetry

Three epochs of spectropolarimetry were obtained of SN 2015U near peak brightness utilising the dual-beam polarimetry mode of the Lick 3 m Kast spectrograph. The orientation of the slit on the sky was always set to a position angle of  $180^\circ$  (i.e., aligned north-south), and exposures of 900 s were obtained at each of four waveplate positions ( $0^\circ$ ,  $45^\circ$ ,  $22.5^\circ$ , and  $67.5^\circ$ ). On each night, several waveplate sequences

<sup>6</sup> <https://github.com/ishivvers/TheKastShiv>

<sup>7</sup> <http://wiserep.weizmann.ac.il/>



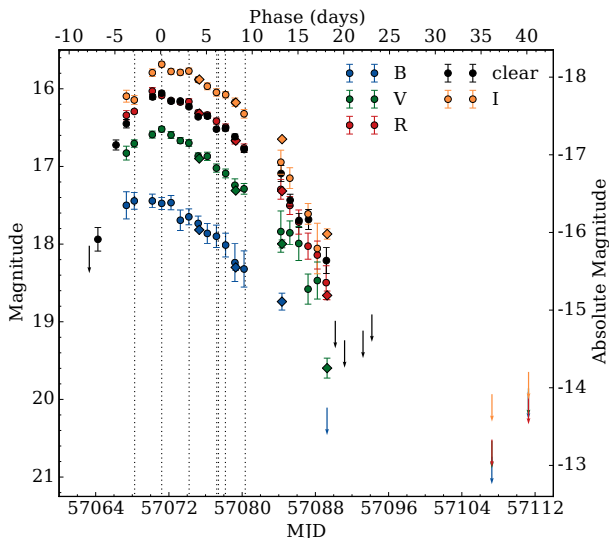


**Figure 2.** The *BVRI* and *clear* passband light curves of SN 2015U after correcting for MW dust absorption but not for the host absorption. KAIT data are indicated by circles and Nickel data by diamonds. The dates of our spectral observations are marked by dotted vertical lines. The phase relative to the *V*-band peak is shown along the top while the absolute magnitude is shown on the right. Because these absolute magnitudes have not been corrected for significant but uncertain dust absorption arising within the host galaxy, they can be taken as lower limits on the luminosity of SN 2015U.

were performed and coadded. Flatfield and arc-lamp spectra were obtained immediately after each sequence without moving the telescope.

For polarimetric calibrations, the low-polarization standard stars BD+32°3739 and BD+05°2618 were observed to verify the low instrumental polarization of the Kast spectrograph. We constrained the average fractional Stokes  $Q$  and  $U$  values to  $< 0.1\%$ . By observing the above unpolarized standard stars through a 100% polarizing filter we determined that the polarimetric response is so close to 100% that no correction was necessary. Finally, we obtained the instrumental polarization position-angle curve and used it to correct the data. We observed the high-polarization stars HD 19820, BD +59°389, and V1Cyg12 to obtain the zero-point of the polarization position angle on the sky ( $\theta$ ) and to determine the accuracy of polarimetric measurements, which were generally consistent with previously published values within  $\Delta P < 0.05\%$  and  $\Delta\theta < 1^\circ$ . All spectropolarimetric reductions and calculations were performed using the methods described by Mauerhan et al. (2015, and references therein), and we define the polarimetric parameters in the same manner as those authors (Stokes parameters  $q$  and  $u$ , debiased polarization  $P$ , and sky position angle  $\theta$ ).

To probe the Galactic component of interstellar polarization (ISP) along the line of sight toward SN 2015U, we used the method of spectroscopic parallax to select three stars within  $1^\circ$  of separation from the source and measured their integrated *V*-band polarization ( $P$ ) and position angle ( $\theta$ ). For HD 58221 we obtained  $P = 0.28\% \pm 0.01\%$ ,  $\theta = 13.0^\circ \pm 0.6^\circ$ ; for HD 58726,  $P = 0.50\% \pm 0.01\%$ ,  $\theta = 24.8^\circ \pm 0.3^\circ$ ; and for HD 59291,  $P = 0.24\% \pm 0.01\%$ ,  $\theta = 16.3^\circ \pm 0.7^\circ$  (un-

certainities are statistical). We interpret the significantly higher value of  $P$  for HD 58726 (A0 V spectral type) as being caused by some intrinsic polarization for that star, so we used the average values of the other two stars (0.25%,  $14.3^\circ$ ) to calculate the associated Serkowski-Whittet form (Serkowski et al. 1975; Whittet et al. 1992), assuming a total-to-selective extinction ratio of  $R_V = 3.1$  and that the polarization peaks at  $5500 \text{ \AA}$ , values appropriate for the MW. The resulting curve was subtracted from the SN 2015U data to remove the small but nonnegligible Galactic component of ISP. The above observations (along with calibration observations of the low-polarization standard star HD 14069 and the high-polarization standards HD 245310 and HD 25443) were taken with the Kast spectrograph on 2015 Sep. 21.

### 3 ANALYSIS

#### 3.1 Dust Corrections

All observations of SN 2015U are heavily affected by an obscuring screen of dust present in the host galaxy, NGC 2388. Because the treatment of dust corrections affects much of the following discussion, we start by describing our efforts to understand, characterise, and correct for the effects of the host-galaxy dust. First, however, we correct for MW dust along the line of sight using the dust maps of Schlafly & Finkbeiner ( $E(B - V) = 0.0498 \text{ mag}$ ; 2011) and assuming  $R_V = 3.1$  (Cardelli et al. 1989).

Ochner et al. (2015) note that a significant amount of host-galaxy reddening is apparent in their classification spectrum, with an estimated  $E(B - V) = 1.0 \text{ mag}$  based upon the Na I D feature. Our higher-resolution DEIMOS spectrum from Feb. 27 reveals complex Na I D absorption near the host redshift (we examine the structure of this feature in §3.2.4). We measure the equivalent width (EW) of the entire absorption complex to be  $9.1 \pm 0.15 \text{ \AA}$  — well outside the empirical relations of Poznanski et al. (2012) and similar previous efforts, which show that the Na I D lines saturate and lose their predictive power above a total EW of  $\sim 2 \text{ \AA}$  and  $E(B - V) \approx 1.0 \text{ mag}$ . This indicates that the reddening toward SN 2015U likely exhibits  $E(B - V) > 1.0 \text{ mag}$ , if the dust in NGC 2388 is similar to that in our MW.

Pastorello et al. (2015c) measure an Na I D EW of  $6.5 \pm 0.5 \text{ \AA}$  from their spectra; we tentatively suggest that the discrepancy between their value and ours is caused by different choices made when defining the local continuum. Figure 6 shows that the Na I D components fall on the red wing of the He I emission line, even at early times. However, if one instead defines the local continuum based upon the overall flux-density level (a reasonable choice if the emission-line wings were not detected), one obtains Na I D EW values similar to those of Pastorello et al. (2015c).

We next examined the  $5780.5 \text{ \AA}$  diffuse interstellar band (DIB). This feature is one of the strongest DIBs; it has long been known to correlate with extinction in the MW when the Na I D feature is saturated (e.g., Herbig 1995; Friedman et al. 2011; Lan et al. 2015; Baron et al. 2015), and Phillips et al. (2013) show a clear correlation between this feature and the reddening toward SNe Ia produced by host-galaxy dust. We do not detect this feature, and our spectra have insufficient S/N to place strong constraints on the

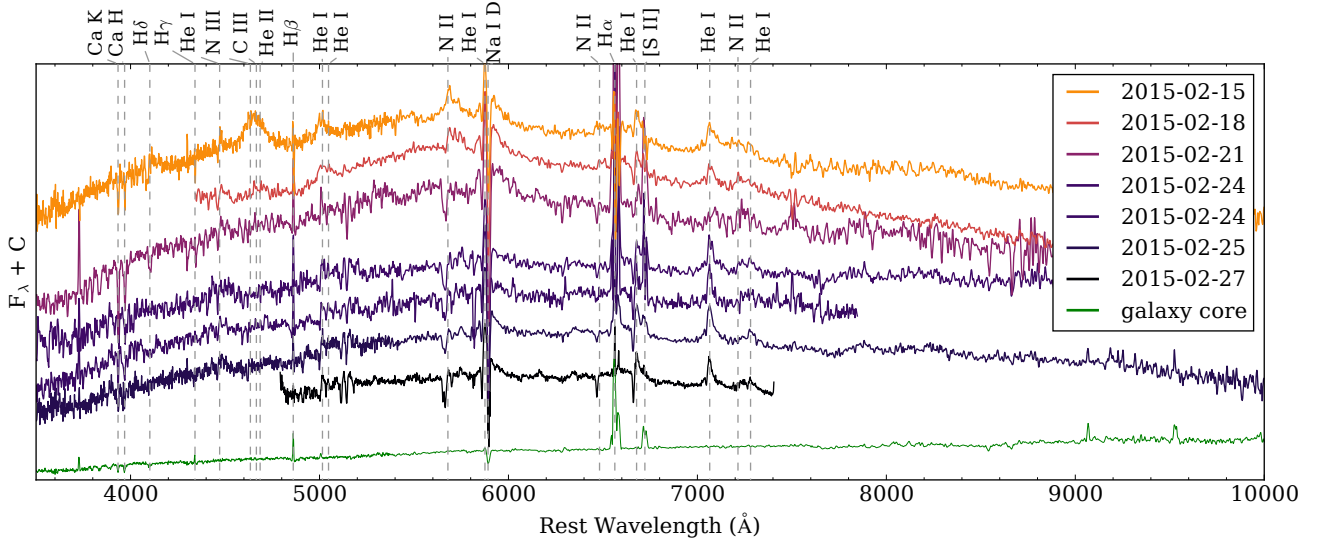


**Figure 3.** The spectral sequence of SN 2015U. This figure shows the spectral evolution after dereddening to correct for MW dust absorption but not for the host-galaxy absorption. On the bottom, we show an extraction of NGC 2388’s nucleus, taken from a Kast spectrum obtained on Feb. 15. Contamination from the host galaxy’s strong emission lines is apparent in some spectra; we indicate H $\alpha$ , H $\beta$ , and [S II]  $\lambda$ 6716, 6731, as well as the host’s Na I D absorption.

**Table 2.** Journal of Spectroscopic Observations

| UT Date                     | Type <sup>a</sup> | Tel./Instr. | Wavelength<br>(Å) | Resolution<br>(Å) | Exp.<br>(s)              | Observer <sup>b</sup> | Reducer <sup>b</sup> |
|-----------------------------|-------------------|-------------|-------------------|-------------------|--------------------------|-----------------------|----------------------|
| 2015-02-15.256              | F                 | Shane/Kast  | 3440–10,870       | 2                 | 1200                     | IS                    | IS                   |
| 2015-02-18.211              | F                 | Shane/Kast  | 4400–9880         | 2                 | 2400                     | WZ                    | IS                   |
| 2015-02-21.207              | F                 | Shane/Kast  | 3500–10,500       | 2                 | 1200                     | WZ                    | IS                   |
| 2015-02-21.313              | S                 | Shane/Kast  | 4500–10,000       | 16                | 4 × 4 × 900 <sup>c</sup> | WZ                    | JM                   |
| 2015-02-24.224              | F                 | Shane/Kast  | 3500–10,500       | 2                 | 1200                     | WZ                    | IS                   |
| 2015-02-24.322              | S                 | Shane/Kast  | 4500–10,000       | 16                | 3 × 4 × 900 <sup>c</sup> | WZ                    | JM                   |
| 2015-02-24.414              | F                 | Shane/Kast  | 3500–7875         | 1                 | 1800                     | WZ                    | IS                   |
| 2015-02-25.171              | F                 | Shane/Kast  | 3500–10,500       | 2                 | 1200                     | MG                    | MG                   |
| 2015-02-25.301              | S                 | Shane/Kast  | 4500–10,000       | 16                | 5 × 4 × 900 <sup>c</sup> | MG                    | JM                   |
| 2015-02-27.34               | F                 | Keck/DEIMOS | 4850–7510         | 0.3               | 1200                     | PK                    | IS                   |
| 2010-03-022.17 <sup>d</sup> | F                 | Shane/Kast  | 3450–10,790       | 3                 | 2100                     | IK                    | JS                   |

<sup>a</sup> F: total flux; S: spectropolarimetry.

<sup>b</sup> Observers and data reducers are indicated with their initials. IS: Isaac Shivvers; WZ: WeiKang Zheng; JM: Jon Mauerhan; MG: Melissa Graham; PK: Patrick Kelly; IK: Io Kleiser; JS: Jeffrey Silvean.

<sup>c</sup> All spectropolarimetry was obtained by rotating multiple times through four waveplate positions; see §2.3.

<sup>d</sup> A previously unpublished observation of SN 2010al; see Figure 13.

dust using our nondetection. We also examined modeled estimates for the amount of dust obscuring the bulk of stars in the host galaxy NGC 2388 (Pereira-Santaella et al. 2015), and we determined the same value at the location of the SN (within  $\sim 1''$  on the sky) by measuring the Balmer ratio implied by the H $\alpha$  and H $\beta$  galaxy lines present in our DEIMOS spectrum (e.g., Brocklehurst 1971). We estimate  $E(B - V) \approx 0.56$  and 1.1 mag, respectively, toward the average star in NGC 2388’s core and the average star near the explosion site of SN 2015U. Although this does not provide a measure of the line-of-sight reddening toward SN 2015U specifically, it does provide valuable context about the dust content of NGC 2388.

Additional information is available to us through the spectropolarimetry: as we describe in §3.2.5, the peak of the polarization spectrum ( $\lambda_{\max}$ ) of NGC 2388’s ISM is blueward of 4600 Å. The shapes of the polarization law and the dust-extinction law are related within the MW (e.g., Serkowski et al. 1975; Clayton & Mathis 1988). Using  $R_V = (-0.29 \pm 0.74) + (6.67 \pm 1.17) \lambda_{\max}$  from Clayton & Mathis (1988, with  $\lambda_{\max}$  in  $\mu\text{m}$ ), our measurement of  $\lambda_{\max} < 0.46 \mu\text{m}$  implies  $R_V < 2.8 \pm 0.9$ . However, note that Patat et al. (2015) show the polarization properties of the host-galaxy dust obscuring several well-studied and reddened SNe Ia to be remarkably different from those of the dust in our MW.

Finally, we model SN 2015U as a blackbody emitter ob-

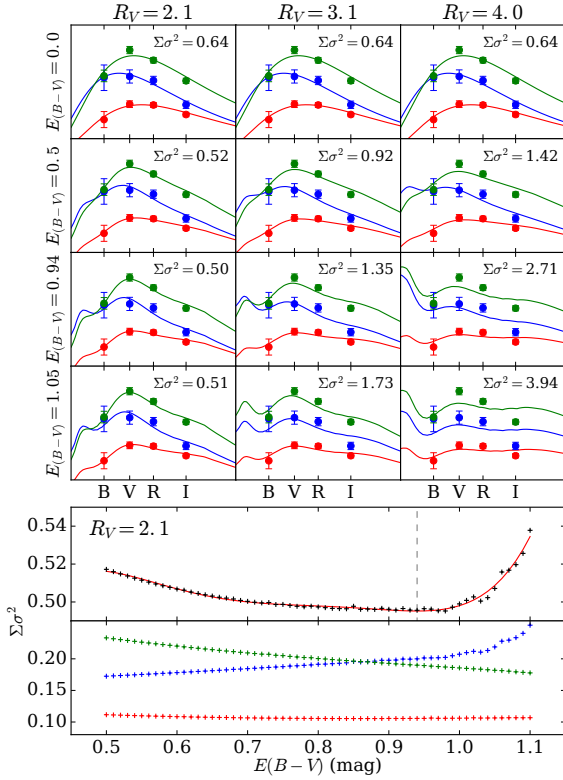


**Figure 4.** In the top panel, we fit reddened blackbodies to our photometry of SN 2015U at three epochs (blue, Feb. 14.35; green, Feb. 18.21; red, Feb. 27.21) after correcting for MW absorption and assuming various values for  $R_V$  and  $E(B-V)$  within NGC 2388. For many data points, the measurement errors are smaller than the plotted symbol. The weighted sum of squared differences ( $\Sigma\sigma^2$ ) between observed photometric points and synthetic photometry of a blackbody is shown in the upper right of each plot; lower values indicate a better agreement across all epochs. In the bottom panel, we show  $\Sigma\sigma^2$  as a function of  $E(B-V)$  for  $R_V = 2.1$  in black as well as  $\Sigma\sigma^2$  broken down by individual epochs, coloured as above.  $R_V = 2.1$  and  $E(B-V) = 0.94^{+0.1}_{-0.4}$  mag (marked with a dashed line in the bottom panel) are the preferred values. In many panels a blue feature is introduced into the reddened blackbody spectrum by the wavelength dependency of the MW’s reddening law, but our spectral data provide no clear evidence for or against such a feature in the spectra of SN 2015U.

scured behind a simple screen of dust in the host galaxy and fit for the parameters of that dust via comparisons with our multiband photometry at three epochs (pre-maximum, maximum, and post-maximum brightness). Our spectra show that the emission from SN 2015U is roughly that of a blackbody obscured by dust, at least at optical wavelengths (unlike most SNe, which display spectra consisting of prominent and overlapping features with sometimes strong line blanketing), and in §3.5 we discuss why one would expect roughly blackbody emission from SN 2015U. We use PySynphot<sup>8</sup> and assume the dust is described by the empirical extinction law of Cardelli et al. (1989) — by varying the parameters  $R_V$  and  $E(B-V)$  we are able to explore a wide variety of dust

populations and search for the parameters that produce the best blackbody fits to our photometric data.

Figure 4 shows a comparison between synthetic photometry from PySynphot and the photometry assuming four different values for  $E(B-V)$  ranging from 0.0 mag to 1.0 mag and three different reddening laws parameterised by  $R_V$  from 2.1 to 4.0 (note that PySynphot only includes a few built-in options for  $R_V$ ; we explore the most relevant of them here). For every combination of  $R_V$  and  $E(B-V)$ , we perform a weighted least-squares fit to determine the best-fit temperature and luminosity of the source blackbody and we list the weighted sum of squared differences ( $\Sigma\sigma^2$ ) for each. Figure 4 shows that a nonzero amount of host-galaxy reddening correction makes the fits worse for  $R_V = 3.1$  and 4.0 — in those cases the photometric data prefer a blackbody with no dust. However, the spectra clearly show a nonthermal rolloff at blue wavelengths (see Figure 3), and so there must be a significant amount of dust absorption within NGC 2388. If we instead adopt  $R_V = 2.1$ , a grid search over  $E(B-V)$  values indicates a best fit at  $E(B-V) \approx 0.94$  mag. As Figure 5 shows, dereddening the spectra for this reddening law appears to correct the blue rolloff. Figure 4 shows that  $\Sigma\sigma^2$  increases above  $E(B-V) = 1.0$  and below  $E(B-V) = 0.6$  mag, but between those values  $\Sigma\sigma^2$  is only weakly dependent upon  $E(B-V)$ . We therefore use Figure 4 to estimate our error bars:  $E(B-V) = 0.94^{+0.1}_{-0.4}$  mag. A similar approach was taken by Pastorello et al. (2015c), who compared the colour curves of SN 2015U to the intrinsic colour curves of other SNe Ibn to obtain  $E(B-V)_{\text{tot}} = 0.81 \pm 0.21$  mag (assuming  $R_V = 3.1$ ). However, as they note, the SN Ibn subclass is remarkably heterogeneous, and it is not clear whether the physics governing those colour curves is the same for all members.

Given the above discussion, we adopt  $R_V = 2.1$  and  $E(B-V) = 0.94^{+0.1}_{-0.4}$  mag. The large EWs measured from the NaID and the odd absorption-feature complex indicate that a simple analysis of those features cannot be trusted. Studies of the integrated galaxy flux and the Balmer decrement measured from our spectrum show that the bulk of NGC 2388’s stellar mass is strongly obscured, and our spectropolarimetric data indicate that SN 2015U itself exploded behind a significant dust screen. The low  $\lambda_{\text{max}}$  value in the polarization spectrum and our blackbody fits to the light curves together prefer a relatively wavelength-dependent dust extinction law for NGC 2388 (i.e.,  $R_V < 3.1$ ) and  $E(B-V) = 0.94^{+0.1}_{-0.4}$  mag — we find this line of reasoning most convincing. The above result is consistent with the  $E(B-V) = 0.99 \pm 0.48$  mag adopted by Pastorello et al. (2015c), though they assume  $R_V = 3.1$ . Our determination of the dust properties toward SN 2015U remains uncertain, so we consider a range of plausible reddening corrections throughout the rest of this paper. We find that the extinction toward §3.2.4 does not appear to change over the course of our observations, and we discuss and reject the possibility that a significant fraction of the extinction toward SN 2015U arises from the SN’s CSM rather than the host galaxy’s ISM.

### 3.2 Spectra

The optical spectra of SN 2015U show a strong continuum overlain with narrow and intermediate-width emission features. Though our data cover only 12 days of SN 2015U’s evolution, they range from a pre-maximum spectrum to one

<sup>8</sup> <http://ssb.stsci.edu/pysynphot/docs/>

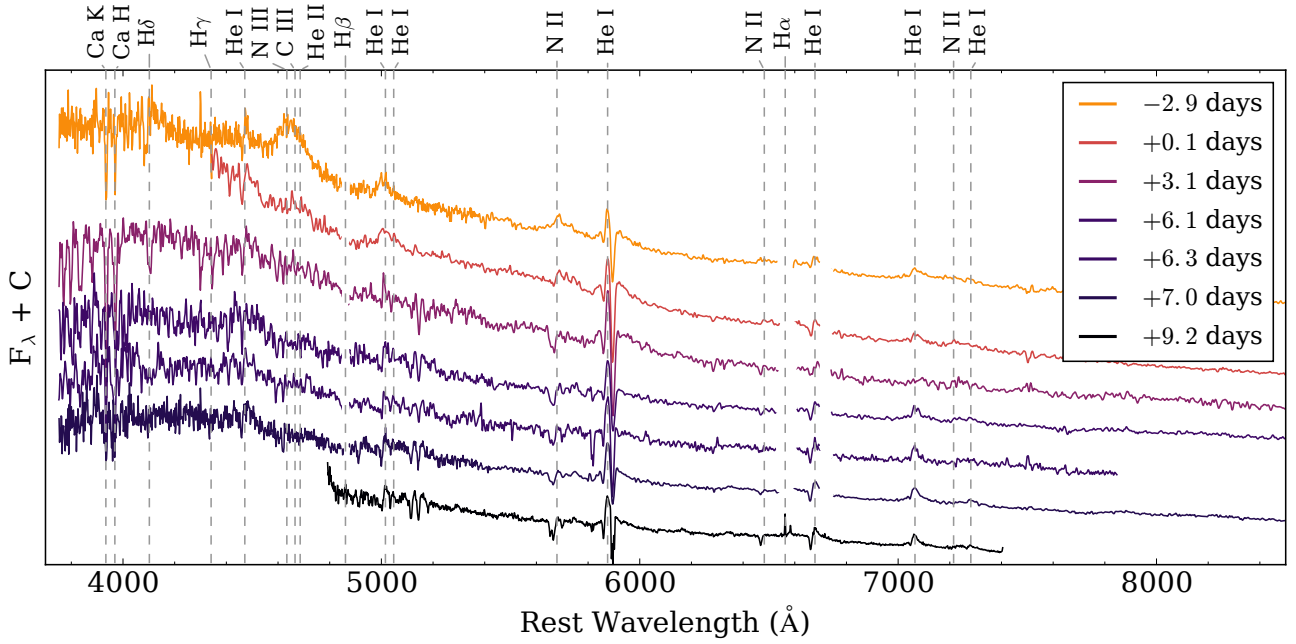


**Figure 5.** The spectral sequence of SN 2015U after dereddening to correct for MW dust absorption and the (uncertain) host absorption. Phases are listed relative to the V-band peak brightness. We have masked regions of our low-resolution spectra where the host's narrow emission lines dominate, but we do not mask the NaID absorption features from the MW and the host.

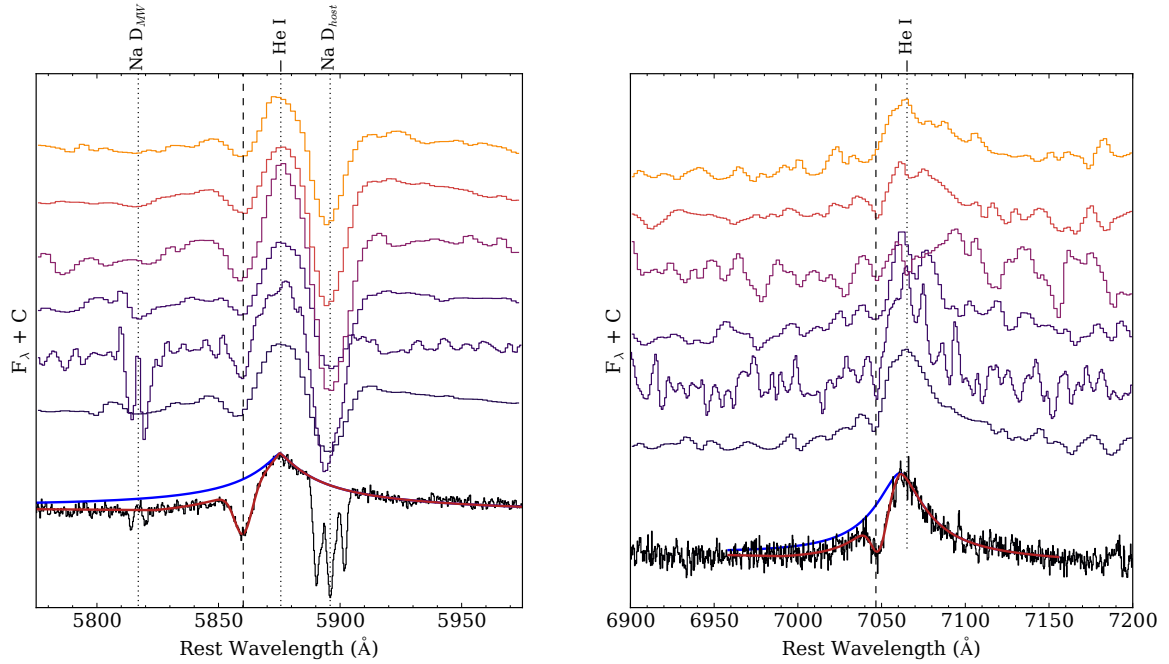


**Figure 6.** The evolution of the He I  $\lambda 5876$  (left) and  $\lambda 7065$  (right) lines. The spectra increase in time downward on the plot as in Figure 3. The rest wavelength of each line is shown with a dotted line and the absorption component is marked at a blueshift of  $v = 789 \text{ km s}^{-1}$  (the mean blueshift of He I lines measured from our DEIMOS spectrum). In the left panel we also mark the host and MW NaID absorption features (see §3.2.4 for a discussion of the host galaxy's remarkable NaID absorption complex).



taken after the SN had faded from peak by  $\sim 1$  mag (see Figure 2). No broad ejecta features became apparent in our spectra throughout that timespan — markedly different behaviour from that of the well-observed, rapidly fading SNe 2002bj, 2005ek, and 2010X (Poznanski et al. 2010; Drout et al. 2013; Kasliwal et al. 2010) and similar to that of the interacting SN 2010jl (e.g., Fransson et al. 2014). Though broad features do not emerge, the continuum temperature shows significant evolution, the narrow emission and absorption features evolve, and the relative ionisation states of the detected elements change. While there are no strong H lines, multiple ionisation levels of helium, nitrogen, iron, and perhaps oxygen and carbon are detected, some in both emission and absorption and some in absorption only. Pastorello et al. (2015c) also present a series of spectral observations of SN 2015U. Their data are in good agreement with ours and extend to later epochs, while our (higher-resolution) spectra illustrate new details not apparent previously.

### 3.2.1 Evolving Line Profiles

The most obvious features in our spectra are emission lines of He I. These lines are centred at the rest wavelength, exhibit a relatively broad base with a full width near zero intensity (FWZI) of  $\sim 9000\text{--}10,000\text{ km s}^{-1}$ , and are overlain with P-Cygni absorption features blueshifted by  $\sim 745\text{ km s}^{-1}$  and with widths of  $400\text{--}500\text{ km s}^{-1}$ . The wavelengths and widths of these features do not significantly change during the  $\sim 12$  days covered by our spectra. We find that the He I line profiles can be parameterised by a “modified Lorentzian” emission component (where the exponent is allowed to vary) with a suppressed blue wing and an overlain Gaussian absorption component, indicative of recombination lines broadened via electron scattering within the CSM. SN 2015U’s line profiles are very similar to those observed in many SNe IIn but with a faster inferred CSM velocity (see, e.g., the spectra of SN 1998S; Leonard et al. 2000; Anupama et al. 2001; Fiasia et al. 2001; Chugai 2001; Shivvers et al. 2015). Figure 6 shows our best fit to the He I  $\lambda 5876$  line using this parameterisation. We also show the unsuppressed Lorentzian feature to emphasise the asymmetry, which arises from the effects of Compton scattering within a wind-like CSM (e.g., Auer & van Blerkom 1972; Hillier 1991; Chugai 2001). The magnitude of the effect scales with the expansion velocity, explaining the strongly asymmetric emission lines of SN 2015U compared to those observed in most SNe IIn.

After He I (and host-galaxy H $\alpha$  and [N II]), the most clearly detected features in our spectra are the N II lines. As Pastorello et al. (2015c) note, SN 2015U appears to be the first SN Ibn to show these features, though they are commonly found in the spectra of hot stars. In our DEIMOS spectrum we are able to identify nine N II absorption lines (see §3.2.3), and for the strongest of these we track their evolution throughout our spectral series. In our  $-2.9$  and  $+0.1$  d spectra, the  $5667\text{ \AA}$  and  $5676\text{ \AA}$  features are apparent in emission around  $v \approx 0\text{ km s}^{-1}$ , but they transition into absorption at  $v \approx 680\text{ km s}^{-1}$  after maximum light — see Figure 7. The same trend is apparent in the N II features at  $6482\text{ \AA}$  and  $7215\text{ \AA}$  (Figure 3).

We find a strong emission feature centred around  $4650\text{ \AA}$  in our earliest spectrum. In Figure 3 we label it as a blend of N III, C III, and He II, a blend that has been observed

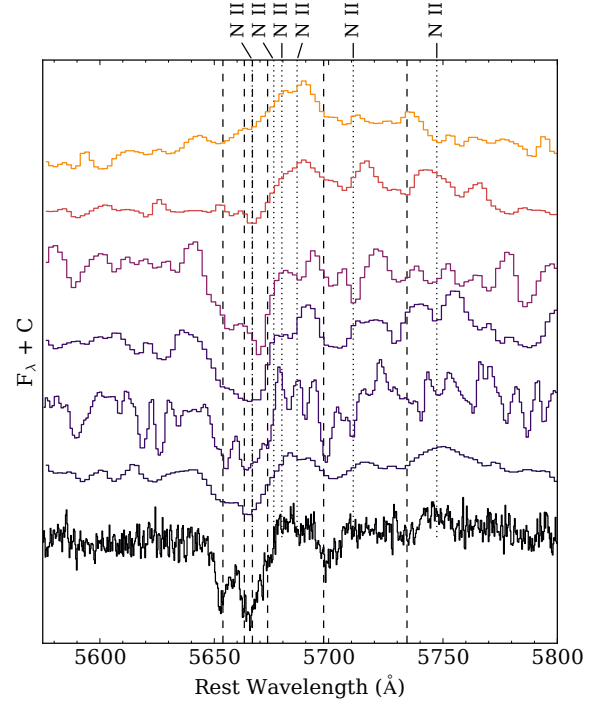


**Figure 7.** The evolution of the N II lines. The spectra increase in time downward as in Figure 3. Identified N II lines are marked at rest using dotted lines and with a blueshift of  $v = 680\text{ km s}^{-1}$  using dashed lines (the mean blueshift of N II lines measured from our DEIMOS spectrum). The emission features marginally detected at  $v = 0\text{ km s}^{-1}$  in our earliest spectra evolve into blueshifted absorption lines post-maximum brightness.

and modeled in the spectra of a few other young, interacting SNe (e.g., Gal-Yam et al. 2014; Shivvers et al. 2015; Pastorello et al. 2015a). The  $4650\text{ \AA}$  emission feature fades rapidly. Given the clear detection of N II at all epochs we believe the identification of N III to be very robust, but whether the blue wing of that emission feature is caused by C III or He II is more difficult to determine. The He II  $\lambda 5411$  line is extremely weak in SN 2015U, which argues that C III must be contributing to the  $4650\text{ \AA}$  feature, but discerning between these ions likely requires detailed modeling and is beyond the scope of this paper.

### 3.2.2 A Trace of Hydrogen?

Inspection of our two-dimensional (2D) spectral images reveals host-galaxy emission features at H $\alpha$ , H $\beta$ , and H $\gamma$ , and there is no indication of either absorption or emission features intrinsic to SN 2015U for any of those lines. However, our spectra at  $-2.1$  d and  $+3.1$  d do show an absorption feature near the expected wavelength of H $\delta$ , decelerating over those 5 days from  $-1060 \pm 75\text{ km s}^{-1}$  (blueshifted) to  $160 \pm 65\text{ km s}^{-1}$  (redshifted relative to the rest frame of SN 2015U, consistent with the rest frame of NGC 2388) and then disappearing by  $+6.1$  d. Though this feature is difficult to disentangle from the significant noise at these wavelengths, it appears to show weak P-Cygni emission in our first observation.

NGC 2388 shows some H $\delta$  absorption, and the fea-

ture from +3.1 d is probably associated with the galaxy (this spectrum has undergone host-galaxy subtraction as described in §2.2). However, in our −2.1 d spectrum SN 2015U was well-separated from the host and we performed no galaxy subtraction. Along with the  $\sim 1000 \text{ km s}^{-1}$  Doppler shift and faint P-Cygni feature, this indicates that the weak H $\delta$  feature in the earliest spectrum of SN 2015U arose within the same CSM as the He I and other features described above.

Several SNe have been found to exist between the II $n$  and Ib $n$  subclasses, exhibiting weak hydrogen features (e.g., SNe 2005la, 2010al, and 2011hw; Pastorello et al. 2008b, 2015a). Remarkably, SN 2010al had an H $\delta$  feature of comparable strength to its H $\alpha$  emission while showing only faint traces of H $\beta$  and H $\gamma$  emission — perhaps similar physics governs the hydrogen emission lines in SN 2015U. Regardless of this putative H $\delta$  feature, the amount of hydrogen in the CSM surrounding SN 2015U must be vanishingly small.

### 3.2.3 Higher Resolution

Our DEIMOS spectrum from Feb. 27 ( $R \approx 5000$ ) reveals fully resolved absorption and emission lines from a host of ions in the spectra of SN 2015U; see Figure 8 and Table 3. We include measured positions and widths for several lines for which we have no good identification; it is especially difficult to differentiate between Fe III ( $E_i = 30.651 \text{ eV}$ ) and Fe II ( $E_i = 16.20 \text{ eV}$ ).<sup>9</sup> In our spectrum we find at least four Fe absorption lines between 4900 and 5200 Å (in the SN rest frame). The strongest two were identified as Fe III by Pastorello et al. (2015c), but several known Fe II lines occur at very similar wavelengths, and we also identify weak features at 4912.5 and 5180.3 Å which are most plausibly interpreted as Fe II  $\lambda 4924$  and Fe II  $\lambda 5195$ . However, these identifications are tentative at best, given the nondetection of other expected Fe II lines and the odd relative strengths of these features, and so we caution the reader against overinterpreting the Doppler velocities presented in Table 3.

We also find three unidentified emission features in our DEIMOS spectrum that are not from host-galaxy contamination, falling near 5290, 6165, and 6340 Å and exhibiting widths similar to those of the He I lines. None of these is clearly detected in our other spectra or the spectra published by Pastorello et al. (2015c, though generally they exhibit a S/N too low to rule them out). The feature at 6340 Å is suggestive of the [O I]  $\lambda\lambda 6300, 6364$  doublet that regularly arises in nebular spectra of stripped-envelope SNe (Types Ib/c; e.g., Filippenko 1997; Matheson 2001), but this identification is only tentative.

### 3.2.4 The Na D Lines

Our DEIMOS spectrum of SN 2015U reveals a remarkable set of Na D absorption lines — see Figure 9. In addition to the MW doublet we find several overlapping lines from NGC 2388 along our sight line, though as we show below, there is no evidence that any of these lines originate within

**Table 3.** Absorption Lines in the DEIMOS Spectrum

| Ion                | Rest $\lambda$<br>(Å) | Observed $\lambda$<br>(Å) | Offset<br>( $\text{km s}^{-1}$ ) | FWHM<br>( $\text{km s}^{-1}$ ) |
|--------------------|-----------------------|---------------------------|----------------------------------|--------------------------------|
| He I               | 5015.7                | 5002.6                    | 778.8                            | 586.4                          |
| He I               | 5047.7                | 5034.6                    | 783.2                            | 267.8                          |
| He I               | 5875.6                | 5860.2                    | 789.2                            | 488.7                          |
| He I               | 6678.2                | 6661.7                    | 737.2                            | 470.1                          |
| He I               | 7065.2                | 7047.9                    | 733.7                            | 432.9                          |
| He I               | 7281.3                | 7265.4                    | 655.9                            | 404.0                          |
| N II               | 5666.6                | 5653.0                    | 721.4                            | 232.5                          |
| N II               | 5676.0                | 5665.4                    | 559.2                            | 433.1                          |
| N II               | 5710.8                | 5699.9                    | 570.4                            | 407.2                          |
| N II               | 5747.3                | 5734.8                    | 651.6                            | 367.5                          |
| N II               | 6482.1                | 6468.1                    | 643.4                            | 428.1                          |
| N II               | 5941.6                | 5927.5                    | 711.5                            | 600.7                          |
| N II               | 6796.6                | 6781.8                    | 654.2                            | 337.9                          |
| N II               | 7214.7                | 7195.9                    | 783.5                            | 173.7                          |
| N II               | 6384.3                | 6366.7                    | 829.6                            | 253.7                          |
| Fe II <sup>a</sup> | 4923.9                | 4912.5                    | 698.0                            | 677.2                          |
| Fe II <sup>a</sup> | 5126.2                | 5114.9                    | 658.1                            | 514.5                          |
| Fe II <sup>a</sup> | 5157.3                | 5143.2                    | 819.4                            | 584.9                          |
| Fe II <sup>a</sup> | 5195.5                | 5180.3                    | 873.2                            | 545.7                          |
| ?                  | —                     | 6197.2                    | —                                | 166.9                          |
| ?                  | —                     | 6207.3                    | —                                | 152.7                          |
| ?                  | —                     | 6285.9                    | —                                | 153.8                          |
| ?                  | —                     | 7206.5                    | —                                | 190.5                          |

Identifications and properties of the absorption lines identified in our DEIMOS spectrum (after correcting for  $z = 0.013161$ ). All lines were fit by a Gaussian with a linear approximation to the nearby continuum, and rest wavelengths were downloaded from the NIST ASD. Characteristic error bars are  $\sim 0.6 \text{ Å}$  ( $30 \text{ km s}^{-1}$ ) for the observed wavelengths and  $\sim 1.6 \text{ Å}$  for the Gaussian FWHM ( $85 \text{ km s}^{-1}$ ), as estimated by calculating the 95% confidence intervals for the N II  $\lambda 5711$  line using MCMC techniques.

<sup>a</sup> It is difficult to determine exactly which Fe II or Fe III transition is responsible for these lines, and so the listed Doppler offsets are only tentative.

the CSM immediately surrounding SN 2015U. The astronomical Na D doublet has been studied in great detail (it was one of the original Fraunhofer lines) and the relative strength of the doublet has long been used to measure the interstellar abundance of neutral sodium: the Na D<sub>2</sub> line is generally observed to be stronger than the D<sub>1</sub> line by a factor ranging from 1.0 to 2.0, for high and low column densities of Na I, respectively (e.g., Strömberg 1948; Nachman & Hobbs 1973; Somerville 1988). The MW Na D doublet in our spectra exhibits the expected behaviour, with an EW ratio of  $D_2/D_1 \approx 1.2$ , but the host-galaxy lines do not.

There are at least two distinct and overlapping Na D absorption doublets near the host-galaxy’s rest frame in the spectrum of SN 2015U. Figure 9 shows them (as well as model fits) in detail. We model the absorption complex by overlaying the modified Lorentzian emission-line profile (see §3.2.1) with two doublets of Voigt absorption profiles (though we note that some of these lines may be unresolved and saturated). D<sub>1</sub> and D<sub>2</sub> lines from a single doublet are forced to have the same velocity properties and to be separated by  $5.97 \text{ Å}$ , but they are allowed independent strengths.

In the top panel of Figure 9 we show the result when we

<sup>9</sup> All ionisation energies and line wavelengths were found through the NIST Atomic Spectra Database (ASD): <http://www.nist.gov/pml/data/asd.cfm>.

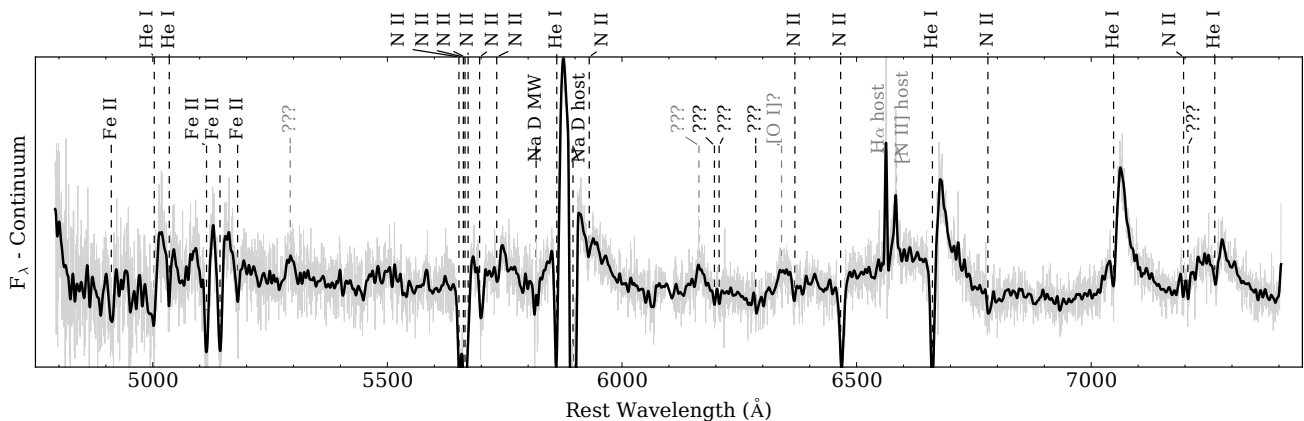


**Figure 8.** The DEIMOS spectrum from Feb. 27 in detail. A simple polynomial continuum fit has been removed. The full spectrum is shown in grey in the background while the black line displays the spectrum smoothed with a  $10 \text{ \AA}$  Gaussian kernel. Identified emission lines are shown with grey dashed lines and text; absorption lines are in black. All absorptions are indicated with a  $745 \text{ km s}^{-1}$  blueshift but emission lines are marked at rest velocity.

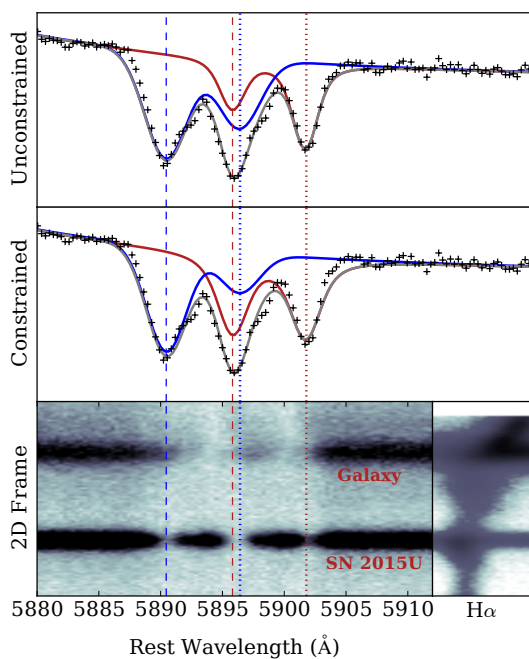


**Figure 9.** The NaD features in our DEIMOS spectrum of SN 2015U and NGC 2388. The top panel plots the observed spectrum of SN 2015U with our best-fit absorption profiles while the middle panel shows the result after introducing the additional constraint that  $D_2/D_1 \geq 1.0$  (see §3.2.4). The shorter-wavelength doublet is shown in blue and the longer-wavelength one in red, with the central wavelengths indicated by dashed and dotted vertical lines for  $D_2$  and  $D_1$ , respectively. Their sum is given in grey. The bottom panel shows the 2D frame of our DEIMOS observation in this region, including both the light from the host and the SN, as well as a cutout of the H $\alpha$  emission line (plotted with the same Doppler  $\delta v$  per pixel) to indicate the shape of the galaxy’s rotation curve.

allow the relative strengths of the doublet (i.e.,  $D_2/D_1$ ) to vary freely. In the rest frame of the SN, the bluest doublet falls at  $\lambda\lambda 5890.45, 5896.35 \pm 0.066 \text{ \AA}$ . This is a blueshift of only  $\sim 25 \text{ km s}^{-1}$  from the SN rest frame, and so this doublet is likely to arise from the ISM of NGC 2388 along our sight line to SN 2015U. The second (redder) doublet, however, falls at  $\lambda\lambda 5895.80, 5901.69 \pm 0.063 \text{ \AA}$  — redshifted from the SN by almost  $300 \text{ km s}^{-1}$ , and even redshifted from the galaxy core by more than  $100 \text{ km s}^{-1}$ . This is within the velocity range of NGC 2388’s rotation curve, but SN 2015U is located well away from the receding spiral arm and the bulk of the galaxy’s receding material (see Figure 1). In addition, the second NaD doublet shows a strength ratio of  $D_2/D_1 \approx 0.5$ , well outside the commonly observed values of  $\sim 1.0\text{--}2.0$  (in contrast, the blue doublet exhibits a reasonable  $D_2/D_1 \approx 1.5$ ).

If, instead, we constrain the doublet ratio to  $D_2/D_1 \geq 1.0$ , we can also obtain a reasonable fit, though this introduces noticeable discrepancies in the reddest part of the feature — see the middle panel of Figure 9. In addition, this forces the doublet ratio of the bluer doublet outside of the range of normal values:  $D_2/D_1 \approx 2.5$ . Adding more components to our model fit will not solve this quandary (though the data do show a shoulder on the bluer doublet, suggesting a third absorption component). The implications for the Na I gas (and the dust) in NGC 2388 are not clear.

Given the spectral signatures of dense CSM surrounding SN 2015U, it is natural to wonder whether some of the NaD absorption arises within the local CSM. Variation in the NaD features over the timescale of the SN evolution would be a clear signature of local absorption (e.g., [Patat et al. 2007](#)); however, as Figure 6 shows, no such variation is apparent in our data.

The bottom panel of Figure 9 displays a cutout of the 2D DEIMOS spectrum around the NaD feature. Both SN 2015U and NGC 2388 are clearly visible, and we also show the rotation curve of the galaxy via a cutout of the H $\alpha$  emission line. The NaD absorption of NGC 2388’s own ISM is seen against the stellar light of the galaxy, and this galactic self-absorption roughly covers the velocity range of

the two components observed along the line of sight toward SN 2015U. It appears that the anomalous red component described above obscures the host galaxy as well as the SN, providing further evidence that this component is unlikely to arise within the CSM of SN 2015U.

### 3.2.5 Spectropolarimetry

We did not observe significant evolution in the polarization of SN 2015U between our three epochs, so we coadded all of the data to increase the S/N; the results are illustrated in Figure 10. The polarization spectrum of SN 2015U appears to be dominated by ISP associated with the host galaxy NGC 2388, showing a strong increase in continuum polarization toward shorter wavelengths with a value of  $P \approx 2.5\%$  at 4600 Å and decreasing to  $P \approx 1.0\%$  near 7000 Å. This behaviour is dissimilar to what is typically observed for the MW ISP, which exhibits a peak and turnover near 5500 Å. Instead, the observed behaviour is reminiscent of the ISP produced by the host galaxies of several SNe Ia, including SNe 1986G, 2006X, 2008fp, and 2014J (Patat et al. 2015, see their Figure 2). The continuous rise in  $P$  beyond the  $B$  and  $U$  photometric passbands has previously been interpreted as evidence for scattering by dust grains smaller than those characteristic of the MW disk ISM.

Interestingly, we observe a significant wavelength dependence for the position angle ( $\theta$ ), which has a value of  $\sim 25^\circ$  at 4600 Å and monotonically trends toward  $\sim 10^\circ$  near 7000 Å. In the MW, the ISP's position angle is generally flat. However, a wavelength dependence in  $\theta$  has been observed along particular lines of sight toward star-forming regions at distances greater than 0.6 kpc (e.g., Gehrels & Silvester 1965; Coyne & Gehrels 1966), and has been explained as the result of photons traversing multiple clouds or scattering media that exhibit various sizes for the scattering particles as well as various orientations for the interstellar magnetic field.

A similar interpretation is plausible here: along the line of sight within NGC 2388 toward SN 2015U there are likely to be multiple separate components of dusty scattering media having different grain sizes and/or different magnetic field orientations. This possibility is particularly interesting considering the complex superposition of multiple NaID absorption doublets that we see in our high-resolution DEIMOS spectrum. If the continuum flux spectrum of SN 2015U is devoid of broad SN features because of high optical-depth CSM, then one might suspect there also to be a separate and distinct scattering component associated with this CSM, if it is dusty. The subsequent re-scattering of this light as it traverses the dusty ISM of the host could provide a means for producing the observed wavelength dependence of  $\theta$ , if there is a difference in grain sizes between these multiple scattering media. Although this scenario is physically plausible, the spectropolarimetric data cannot discriminate between a CSM+ISM scattering combination and multiple components of host ISM, and our analysis of the total-flux NaID features indicates that they are likely associated with ISM (see §3.2.4).

Finally, there is a line-like feature near 5820 Å which might naively be interpreted as a signature of intrinsic polarization associated with SN 2015U and with the He I / NaI transition. However, the MW NaID doublet falls at

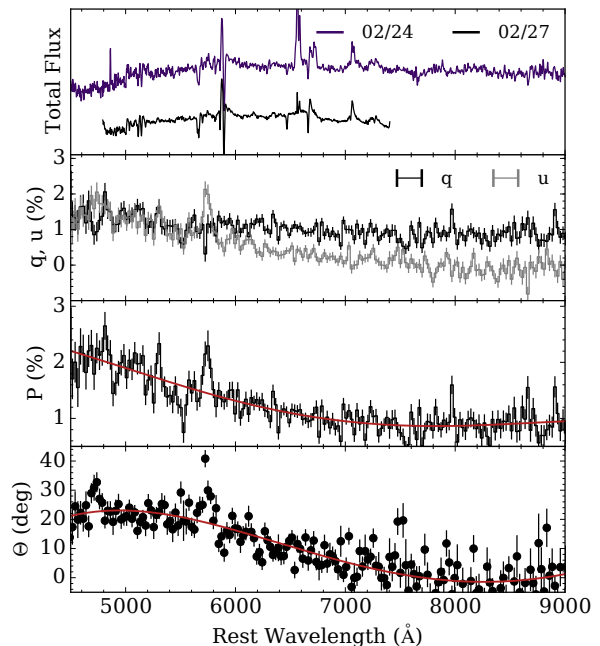


**Figure 10.** Our spectropolarimetric observations of SN 2015U. From top to bottom: total-flux spectra near V-band peak and in higher resolution (for visual comparison),  $q$  and  $u$  Stokes parameters,  $P$  with a fourth-order polynomial fit showing the overall trend, and  $\theta$  with a similar polynomial fit (after discarding outliers). The spectropolarimetric data from three nights of observations have been coadded and binned to 25 Å.

the same wavelength. Although relatively weak compared to the redshifted host-galaxy NaD absorption, the results of our spectral arithmetic in the vicinity of this poorly resolved doublet profile might have created a spurious artifact in the final coadded dataset mimicking the shape of a polarized line feature. Indeed, in each individual epoch, the polarized spectra near this feature appear to suffer from systematic noise, so we are reluctant to attribute this feature to the SN itself.

### 3.3 Photometry

The optical light curves of SN 2015U show that it was a remarkably luminous and rapidly evolving event — Figure 11 shows our photometry corrected for host-galaxy dust reddening. With a peak absolute magnitude of  $\lesssim -19$  mag at optical wavelengths, a rise time of  $\lesssim 10$  d, a time above half-maximum of  $t_{1/2} \approx 12$  d, and a decline rate of nearly  $0.2 \text{ mag day}^{-1}$  after peak, SN 2015U was more than a magnitude brighter than most stripped-envelope SNe and evolved much more rapidly (e.g., Drout et al. 2011; Bianco et al. 2014).

Though the first unfiltered (*clear*) KAIT detection of SN 2015U was on Feb. 11, and it went undetected by KAIT on Feb. 10 ( $> 18.4$  mag), Pastorello et al. (2015c) present detections from Feb. 9 and 10 at  $R = 18.62 \pm 0.26$  and  $18.14 \pm 0.30$  mag, respectively. Unfortunately, the location does not appear to have been observed in the days prior and there



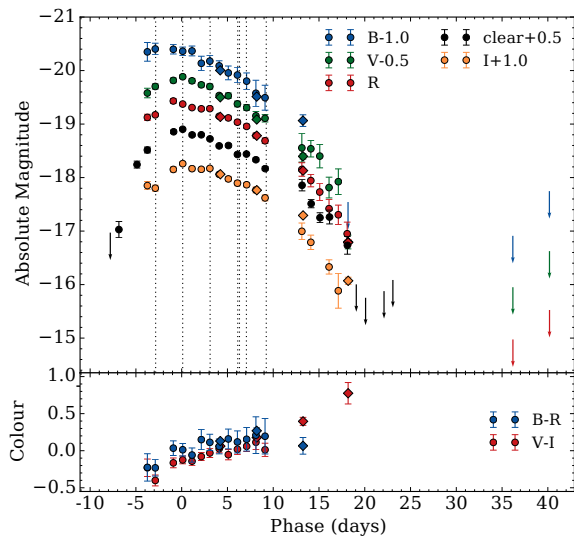


**Figure 11.** The KAIT and Nickel light curves (top) and colour curves (bottom) of SN 2015U, after correcting for MW dust absorption and host absorption. Nickel data are shown with diamonds and KAIT data with circles, and the dates of our spectral observations are indicated in the top panel with dashed vertical lines. Host-galaxy contamination becomes significant in our KAIT photometry around +10 d, and so we only show the Nickel data beyond that date in the lower panel (we include all data in the upper panel). We apply vertical offsets to every passband except *R* in the top panel, to enable comparisons.

are not deep upper limits constraining the explosion date further. SN 2015U rose quite rapidly, so we adopt a tentative explosion date one day before the first detection published by [Pastorello et al. \(2015c\)](#):  $t_{\text{exp}} \approx 57062$  MJD (Feb. 8). This provides us with a rise time for SN 2015U of  $t_{\text{rise}} \approx 9$  days. [Tsvetkov et al. \(2015\)](#) note that SN 2015U is among the most rapidly evolving SNe known, with a decline rate similar to those of SNe 2002bj, 2005ek, and 2010X. We measure  $\Delta M_{15} \approx 2.0$  mag in the *R* band, but note that the decline rate increases ever more steeply after  $\sim 10$  days post-peak, and at all times the bluer passbands decline more rapidly than the red. Simple linear fits indicate the following decline rates before and after +10 d (in mag day $^{-1}$ ):  $B_{\text{early}} = 0.110 \pm 0.007$ ,  $V_{\text{early}} = 0.099 \pm 0.005$ ,  $V_{\text{late}} = 0.28 \pm 0.07$ ,  $R_{\text{early}} = 0.080 \pm 0.005$ ,  $R_{\text{late}} = 0.267 \pm 0.009$ ,  $I_{\text{early}} = 0.067 \pm 0.006$ , and  $I_{\text{late}} = 0.26 \pm 0.04$  (uncertainties are statistical, and our data do not constrain the late *B*-band decline).

SN 2015U is one of the nearest SNe Ibn to date ([Pastorello et al. 2016](#)), but it is still relatively distant for direct progenitor studies (and is obscured by the dust in NGC 2388). Regardless, the *HST* nondetections presented in §2.1 can be used to place interesting constraints on the SN’s progenitor. We compared these limits to the MIST stellar evolutionary tracks ([Choi et al. 2016](#)) at solar metallicity generated in the WFC3/infrared bandpasses (negligible photometric differences exist between NICMOS/NIC2 and WFC3/IR for *F110W* and *F160W*). Based on these tracks we can eliminate single-star progenitors with initial masses  $M_{\text{ini}} \gtrsim 9 M_{\odot}$  and  $\lesssim 40 M_{\odot}$ . That is, the progenitor would have been either a low-mass star near the core-collapse limit or a highly massive evolved star, possibly in a luminous blue

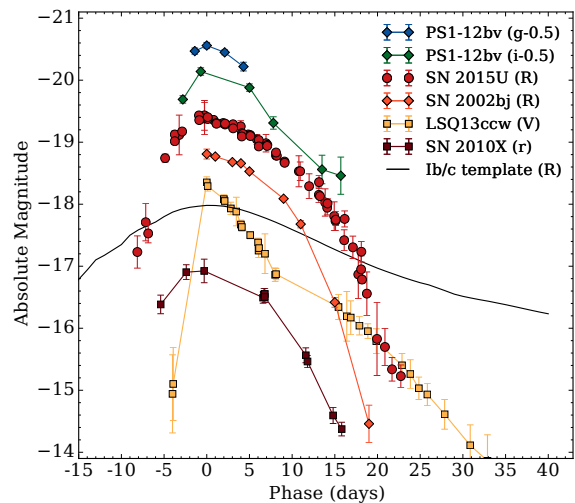


**Figure 12.** The extinction-corrected light curve of SN 2015U compared to light curves of SNe 2002bj and 2010X ([Poznanski et al. 2010](#); [Kasliwal et al. 2010](#)), the rapidly evolving SN Ibn LSQ13ccw ([Pastorello et al. 2015b](#)), and one of the rapidly evolving events from the PS1 sample ([Drout et al. 2014](#)). We also show in black the *R*-band SN Ib/c template from [Drout et al. \(2011\)](#). For SN 2015U we include data from the *R* and *clear* passbands published here as well as the *r*-band photometry from [Pastorello et al. \(2015c\)](#); a vertical offset of  $-0.25$  mag was applied to the *r*-band data to match the *R* and *clear* bands, enabling visual comparison.

variable (LBV) or Wolf-Rayet phase at the time of explosion. We did not interpret our upper limits with respect to existing binary evolution models, and we caution that these results are somewhat dependent upon the uncertain properties of NGC 2388’s dust population.

The structure near SN 2015U’s position in the 1 yr *HST* images (Figure 1) may be due to clumpy star-forming regions, perhaps associated with SN 2015U. NGC 2388 is a strongly star-forming and massive galaxy — [Pereira-Santaella et al. \(2015\)](#) calculate an ongoing star-formation rate of  $\sim 40^{+9}_{-22} M_{\odot} \text{ yr}^{-1}$  and a total stellar mass of  $10^{11.0 \pm 0.1} M_{\odot}$  — and though SN 2015U is not obviously associated with the brightest star-forming regions of the galaxy, our spectra do show emission lines from nearby H II regions. The clump may also be an artifact of the intervening dust lanes in NGC 2388; unfortunately there is essentially no colour information available from our images as the host-galaxy background dominates.

### 3.4 Comparisons with Other Supernovae

In Figure 12 we compare the light curves of SN 2015U to the *R*-band light curves of SN 2002bj ([Poznanski et al. 2010](#)), which was very similar though  $\sim 1$  mag fainter, and SN 2010X ([Kasliwal et al. 2010](#)), which also matches well but was  $\sim 2.5$  mag fainter. SNLS04D4ec and SNLS06D1hc, two of the rapidly rising transients discovered by the Supernova Legacy Survey (SNLS) and presented by [Arcavi et al. \(2016\)](#), also show similar light-curve behaviour but  $\sim 0.5$  mag brighter than SN 2015U (see their Figure 2). In Figure 13 we

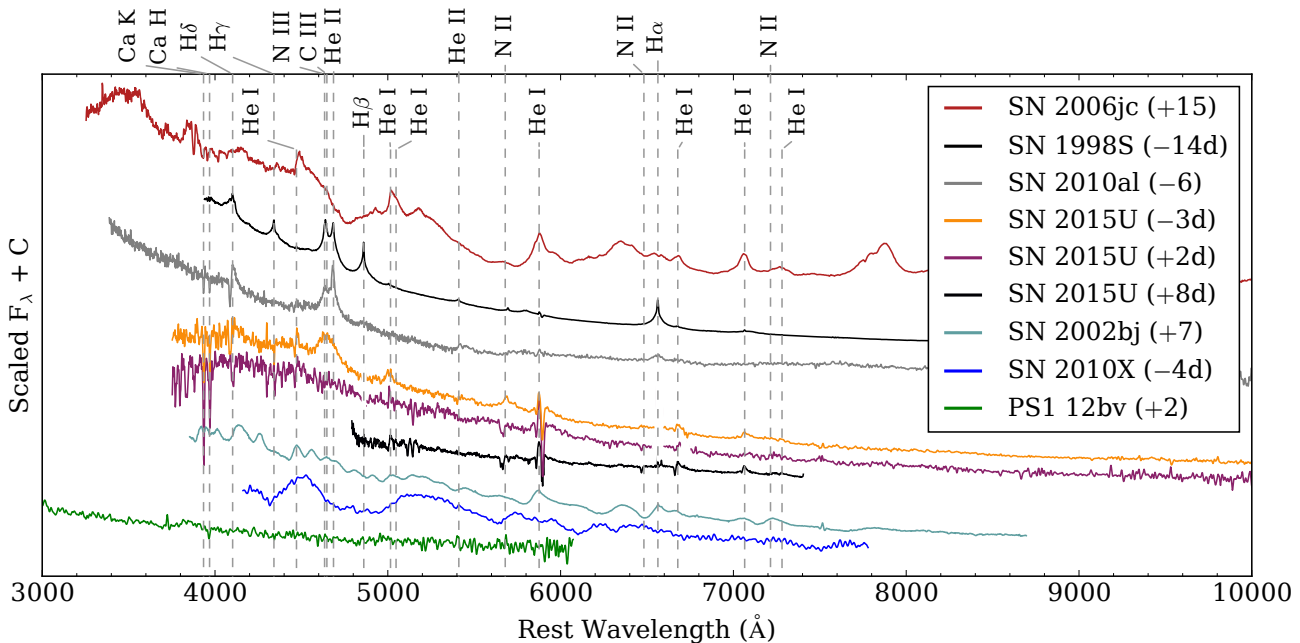


**Figure 13.** Spectra of SN 2015U compared with spectra of the prototypical SN Ibn 2006jc (Foley et al. 2007), the young SN IIn 1998S (Leonard et al. 2000; Shivvers et al. 2015), a previously unpublished spectrum of the transitional SN Ibn 2010al (Silverman et al. 2010; Pastorello et al. 2015a), the rapidly fading SNe 2002bj and 2010X (Poznanski et al. 2010; Kasliwal et al. 2010), and one of the rapidly fading events from the PS1 sample (Drout et al. 2014). Galactic emission features have been masked in the low-resolution spectra of SN 2015U to facilitate comparisons.

compare the spectra of these events: SN 2002bj was hydrogen deficient (SN I Ib-like, though not a good spectroscopic match to normal SNe I Ib) with a strong blue continuum and P-Cygni features at higher velocities than observed in SN 2015U, while SN 2010X showed no hydrogen (SN Ib/c-like, though again not a good spectroscopic match to normal SNe Ib/c) with broad absorption features. (Unfortunately, no spectra were obtained of the SNLS events.)

The light curves and spectra of SN 2015U are quite similar to those of the rapidly evolving and luminous transients discovered in the PS1 dataset and presented by [Drouot et al. \(2014\)](#). Figure 11 includes the  $g$  and  $i$ -band light curves of the relatively well-observed PS1-12bv from that sample; it was discovered at  $z = 0.405$ , so the  $g$  and  $i$  passbands probe rest wavelengths around  $3500 \text{ \AA}$  (about  $100 \text{ \AA}$  shortward of  $B$ ) and  $5350 \text{ \AA}$  (similar to  $V$ ), respectively. Without the  $0.5 \text{ mag}$  offset used in Figure 11, the  $i$ -band light curve of PS1-12bv would overlie the  $V$  band of SN 2015U almost exactly, and the  $g$ -band curve would be somewhat brighter than the  $B$  band of SN 2015U. There are no clear detections of any emission features in the spectrum of PS1-12bv, but it and the other events from the PS1 sample were discovered at very large distances, and high-S/N spectra do not exist for those events. It is plausible that narrow emission lines of helium (and/or hydrogen) were present but went undetected.

Figure 13 shows that SN 2015U shares the blue colour and prominent HeI emission features of the canonical SN Ibn 2006jc (e.g., [Foley et al. 2007](#); [Pastorello et al. 2008a](#)). However, SN 2006jc was discovered post-peak and evolved more slowly than SN 2015U: the earliest extant spectrum of SN 2006jc was taken after the event had faded

$\sim 1$  mag from peak and the spectrum had already transitioned into a nearly nebular phase, though a blue pseudo-continuum was apparent owing to ongoing interaction with the CSM (Foley et al. 2007). At later times, a second red continuum arose in SN 2006jc and the emission features became progressively more asymmetric and blueshifted, evidence for dust formation with the SN system. Increased absorption in the optical passbands by this dust, with re-emission in the infrared, provided an explanation for the rapid increase in the optical decline rate observed for SN 2006jc after  $\sim 50$  days (Mattila et al. 2008; Smith et al. 2008; Pastorello et al. 2008a).

In contrast, SN 2015U presented a spectrum dominated by a single blue continuum through our last epoch of spectroscopy, also taken after the event had faded  $\sim 1$  mag from peak. The  $B-R$  and  $V-I$  colour curves of SN 2015U smoothly trend redward from a few days before (optical) maximum brightness to  $\sim 2$  mag out onto the rapidly fading tail (at which point the SN fades below our detection threshold) — see Figure 11. The accelerating decline rate observed in the SN 2015U light curves does not appear to be due to dust formation: one would expect a redward knee in the colour curves if it were. On the contrary, there is some evidence that the  $B-R$  curve of SN 2015U was beginning to flatten in our last few epochs, though note that  $B$ -band data become sparse.

We also show the light curve of the peculiar and rapidly fading SN Ibn LSQ13ccw in Figure 12 (Pastorello et al. 2015b). LSQ13ccw rose to peak extremely quickly ( $t_{\text{rise}} \approx 5$  d) and then faded rapidly for  $\sim 10$  days, similar to SN 2015U’s behaviour. However, it thereafter slowed in its decline, and the spectra of LSQ13ccw (not shown) exhibited both broad

and narrow features (as do many, but not all, SNe Ibn). The knee in the light curve of LSQ13ccw is plausibly interpreted as evidence for ongoing energy injection from ejecta/CSM interaction in the system — no such knee is observed in the light curve of SN 2015U, which instead appears to be consistent with a single shock-breakout/diffusion event.

The early-time spectrum of SN 2015U is similar to the very early spectra of the Type IIn SN 1998S and the transitional Type IIn/Ibn SN 2010al, excepting the absence of hydrogen (though see §3.2.2 for a discussion of the tentative H $\delta$  feature in SN 2015U). All three events show a smooth, blue, and (approximately) blackbody continuum. The implied CSM velocity of SN 2015U is higher than in SN 1998S and SN 2010al, and SN 2015U shows strong He I lines while the other two events exhibit stronger He II. The N III/C III complex near 4500 Å is clearly detected in all three events — this feature dominates at very early times and disappears by peak (though that evolution took place over different timescales for these SNe).

Despite the spectral similarities, these three SNe displayed diverse light-curve behaviour. SN 1998S had a SN IIL-like light curve with a long-lasting tail (e.g., [Fassia et al. 2000](#)), while the evolution of SN 2010al was more similar to that of SN 2015U though less rapid ([Pastorello et al. 2015a, 2016](#)). The  $B - R$  colour curve of SN 2015U (as shown in Figure 12) is also notably similar to that of SN 2010al, with a slow trend toward redder colours for most of the SN’s evolution and then either leveling off or perhaps even becoming more blue again beyond +10 d and +20 d for SNe 2015U and 2010al, respectively ([Pastorello et al. 2015a](#), see their Figure 4).

The  $\sim 20$ -day timescale for SN 2015U’s evolution and the increasing decline rate are reminiscent of the light curves expected for low- $^{56}\text{Ni}$  explosions in helium-dominated or oxygen-dominated envelopes — see, for example, the models of [Dessart et al. \(2011\)](#) and [Kleiser & Kasen \(2014\)](#). In these models, the recombination of helium or oxygen produces a dramatic and rapid drop in opacity within the ejecta and an inward-moving recombination front. SN 2015U was much more luminous than the objects in these models, but perhaps it was an analogous event wherein a recombination wave in the extended CSM produced a rapid fade from maximum luminosity as the CSM cooled after shock breakout. Similar situations have been observed in hydrogen-rich SNe: there exists a subclass of SNe IIn that shows light curves with a plateau likely produced via hydrogen recombination within their extended CSM (SNe 1994W, 2009kn, and 2011ht; e.g., [Chugai et al. 2004](#); [Kankare et al. 2012](#); [Mauerhan et al. 2013](#)).

The narrow P-Cygni profiles and strong continua of SN 2015U’s spectra are clear indications of dense CSM. The diversity of ways in which such CSM can affect the light curves of SNe has been explored in detail by several authors motivated by observations of SNe IIn/Ibn, superluminous SNe, and rapidly fading SNe (e.g., [Ofek et al. 2010](#); [Chevalier & Irwin 2011](#); [Kleiser & Kasen 2014](#)), and comparisons of SN 2015U’s light curve to these models implies that SN 2015U was a shock-breakout event. The high luminosity indicates that shock breakout occurred at a large radius and that a significant fraction of the SN’s kinetic energy was converted into light, while the lack of a long-lasting light-curve tail shows that the CSM surrounding SN 2015U

was more shell-like than wind-like (there is no interaction-powered tail) and that relatively little  $^{56}\text{Ni}$  was produced (there is no radioactively powered tail).

The rapidly fading light curves of SNe 2002bj and 2010X are remarkably similar to those of SN 2015U, and we argue that their spectral differences do not exclude the possibility that these three events were fundamentally quite similar. By varying the radius of a putative opaque CSM shell in a simple model, we can understand events spanning a range of luminosities and timespans for which the opaque CSM reprocesses the SN flux. Under the assumption that their light curves are all shock cooling curves without significant contribution from radioactive nickel, the peak luminosities and timescales of these three SNe should be governed roughly by

$$t_{\text{SN}} \propto E^{-1/6} M^{1/2} R^{1/6} \kappa^{1/6} T^{-2/3},$$

$$L_{\text{SN}} \propto E^{5/6} M^{-1/2} R^{2/3} \kappa^{-1/3} T^{4/3},$$

following [Kleiser & Kasen \(2014\)](#), adapted from [Kasen & Woosley \(2009\)](#) for hydrogen-free SNe and based on the analytic framework of [Popov \(1993\)](#).  $E$  is the energy of the SN explosion,  $M$  is the mass ejected, and  $R$  is the effective radius (in this case, the radius reached by a significant amount of mass ejected prior to the final explosion).

In particular, consider the peak-luminosity equation, assuming these explosions are similar in all their properties except for the effective pre-SN radius  $R$ , which would be determined by the time before explosion and the speed at which any pre-SN material was ejected. Inverting the equation, the pre-SN effective radius  $R \propto L_{\text{SN}}^{3/2}$ . If we assume that the ejecta velocities of all three objects are similar, this means that the ejecta from the SN itself will pass through the surrounding CSM in a time  $t_{\text{interact}} \propto R$ , and the length of time after explosion we expect to see narrow lines from this interaction is proportional to  $R$ . Comparing the relative peak luminosities, we find that, since SN 2015U exhibited narrow lines at least up to  $\sim 16.5$  days after explosion, SN 2002bj should have shown narrow lines at least until  $\sim 5.5$  days after explosion and the even dimmer SN 2010X would have shown narrow lines at least until  $\sim 0.52$  days. These times are well before the first spectra were taken of either SN 2002bj or SN 2010X. Typically, we expect that to discover narrow lines in these rapidly fading SNe, we will either need to look at the brightest among them or catch them very early. The luminosity (and timescale) may also depend on the explosion energies, ejected masses, and other properties of the SN, but these must be disentangled with more sophisticated numerical approaches.

### 3.5 Temperature and Luminosity Evolution

The extreme and uncertain degree of host-galaxy dust reddening toward SN 2015U makes estimating bolometric properties quite difficult. In §3.1 we assume that the emission from SN 2015U is roughly blackbody in spectral shape; here we further discuss this assumption. It has long been known that the continua of young SNe II exhibit “diluted blackbody” spectral energy distributions (SEDs), which (at optical wavelengths) are similar to the Planck function at a lower temperature (e.g., [Hershkowitz et al. 1986](#); [Eastman et al. 1996](#)). Though SN 2015U is certainly not a SN II, it is

continuum-dominated, and in the sections above we present evidence that SN 2015U was shrouded in an optically thick CSM. In addition, [Moriya et al. \(2011\)](#) show that modeled shock breakouts from the hydrogen-dominated CSM around red supergiants exhibit roughly blackbody SEDs. [Rabinak & Waxman \(2011\)](#) explore shock breakouts from He or He/CO stellar envelopes in detail; for He-dominated stellar envelopes, they show that the colour temperature of the system deviates from the photosphere's temperature by a (time-dependent) factor of only  $\sim 20\%$ , largely owing to diffusion effects as a helium recombination wave moves through the material.

Given the above discussion, we assume that SN 2015U's emission was roughly blackbody and we estimate the bolometric properties by fitting a dust-reddened Planck spectrum to our multiband photometry. Using our almost nightly observations of SN 2015U in the *BVRI* passbands, we assembled the observed optical SEDs from  $-5$  d to  $+20$  d and find the best-fit blackbody temperature, radius, and luminosity using MCMC maximum-likelihood methods. As described in §3.1, there are large uncertainties in the properties of the host galaxy's dust, and these uncertainties produce similarly large uncertainties in the absolute value of the temperature at any given time. In addition, our optical photometry largely probes the Rayleigh-Jeans tail of SN 2015U's SED, so the implied bolometric corrections are large and uncertain. Our MCMC-produced error bars include these effects, and our photometric data do indicate significant temperature evolution (assuming  $E(B - V)$  and  $R_V$  do not change). Because our data constrain the evolution of SN 2015U more strongly than they constrain the absolute values of any given parameter, it is useful to consider the implications for a few assumed values of  $E(B - V)$ .

Figure 14 shows the blackbody temperature, bolometric luminosity, and radius evolution of SN 2015U for three different assumed values of  $E(B - V)$ , adopting  $R_V = 2.1$ . In all cases, the best-fit temperature decreases over time, with the temperature falling rapidly before (optical) peak and then decreasing slowly thereafter. The effective blackbody radius increases with a photospheric velocity of  $v_{\text{phot}} \approx 15,000 \text{ km s}^{-1}$  until peak, leveling off thereafter. Though this value of  $v_{\text{phot}}$  is similar to the characteristic velocities of ejecta in stripped-envelope SNe, our spectra do not show any material moving that quickly and, given our interpretation of SN 2015U as a cooling shock-breakout event, we expect the photospheric radius to be approximately constant throughout these observations. In addition, Figure 14 may surprise the reader by indicating that the peak bolometric luminosity occurred several days before the optical peak. Though the bolometric corrections are at their largest and most uncertain at early times, and we unfortunately do not know of any observations constraining the ultraviolet emission of SN 2015U, similar behaviour was observed from SN Ibn 2010al with ultraviolet to near-infrared wavelength coverage ([Pastorello et al. 2015a](#)).

In addition, we can constrain the temperature evolution of SN 2015U independently of the continuum shape through the relative line strengths of detected emission lines in our spectra. Though detailed modeling is beyond the scope of this paper, the pre-maximum detection and rapid fading of the N III/C III/He II 4500 Å complex in our spectra of SN 2015U brings to mind the spectral evolution of

**Table 4.** Bolometric Properties of SN 2015U

| $E(B - V)$<br>(mag) | $L_{\text{peak}}$<br>(erg s $^{-1}$ ) | $E_{\text{rad}}$<br>(erg) | $T_{\text{peak}}$<br>(K) | $R_{\text{peak}}$<br>(cm) |
|---------------------|---------------------------------------|---------------------------|--------------------------|---------------------------|
| 0.5                 | $7.3 \times 10^{42}$                  | $9.3 \times 10^{48}$      | 8400                     | $1.5 \times 10^{15}$      |
| 0.94                | $5.9 \times 10^{43}$                  | $7.1 \times 10^{49}$      | 19,000                   | $8.7 \times 10^{14}$      |
| 1.05                | $2.3 \times 10^{44}$                  | $2.9 \times 10^{50}$      | 30,000                   | $6.7 \times 10^{14}$      |

Bolometric luminosity, radiated energy, blackbody temperature, and blackbody radius for the three assumed values of  $E(B - V)_{\text{host}}$  shown in Figure 14.

SN 1998S (see Figure 13). Detailed CMFGEN models of SN 1998S while the 4500 Å feature was strong were presented by [Shivvers et al. \(2015\)](#), indicating a temperature of  $\sim 30,000$  K throughout most of the line-forming region. The agreement between this value and the pre-maximum temperatures found for SN 2015U assuming  $E(B - V) = 0.94$  mag are heartening.

In Table 4 we present the integrated energy released and various values at *V*-band peak for three assumed values of  $E(B - V)$ . Our uncertainty about the host galaxy's dust properties is the dominant source of error in this analysis, and the spread over these three values of  $E(B - V)$  indicates the range. All values are estimated through simple polynomial fits to the curves shown in Figure 14. To calculate  $E_{\text{rad}}$ , we integrated from day  $-5$  to day  $+20$  (the timespan of our almost nightly multiband photometric coverage), and for the other parameters we list the value at *V*-band peak. Note that the bolometric luminosity peaks before the optical maximum; again, see Figure 14.

### 3.6 Nickel Content

A slowly declining light-curve tail, powered either via CSM interaction or  $^{56}\text{Ni}$  decay, has been detected in some SNe Ibn, but many members of this subclass (including SN 2015U) do not show one (e.g., [Foley et al. 2007](#); [Gorbikov et al. 2014](#); [Pastorello et al. 2016](#)). For most SNe I, Arnett's law can be used to estimate the total  $^{56}\text{Ni}$  synthesized by the explosion ([Arnett 1982](#)) based upon observed properties near the time of peak luminosity; however, that approach is not applicable for shock-breakout events. If the opacity of the ejecta is well understood, the luminosity at late times can be used instead. For example, [Hamuy \(2003\)](#) analyzed Type IIP supernovae and, given a luminosity  $L_t$  at time  $t$  and an explosion time  $t_0$ , estimated the  $^{56}\text{Ni}$  mass to be

$$M_{\text{Ni}} = (7.866 \times 10^{44}) L_t \exp\left(\frac{(t - t_0)/(1 + z) - 6.1}{111.26 \text{ d}}\right) M_{\odot}.$$

This equation assumes that  $\gamma$ -rays produced via radioactive decay are fully trapped and thermalized by the ejecta, an assumption which (though reasonable for SNe IIP) has been shown not to be true for most stripped-envelope SNe (which fade faster than expected for complete trapping; e.g., [Wheeler et al. 2015](#)).

The extreme CSM surrounding SN 2015U further complicates the issue, as it may be contributing luminosity via ongoing interaction at late times and perhaps even trapping a higher fraction of the  $\gamma$ -rays than is normal for CSM-free SNe Ib/c. Though a robust measure of the amount of nickel



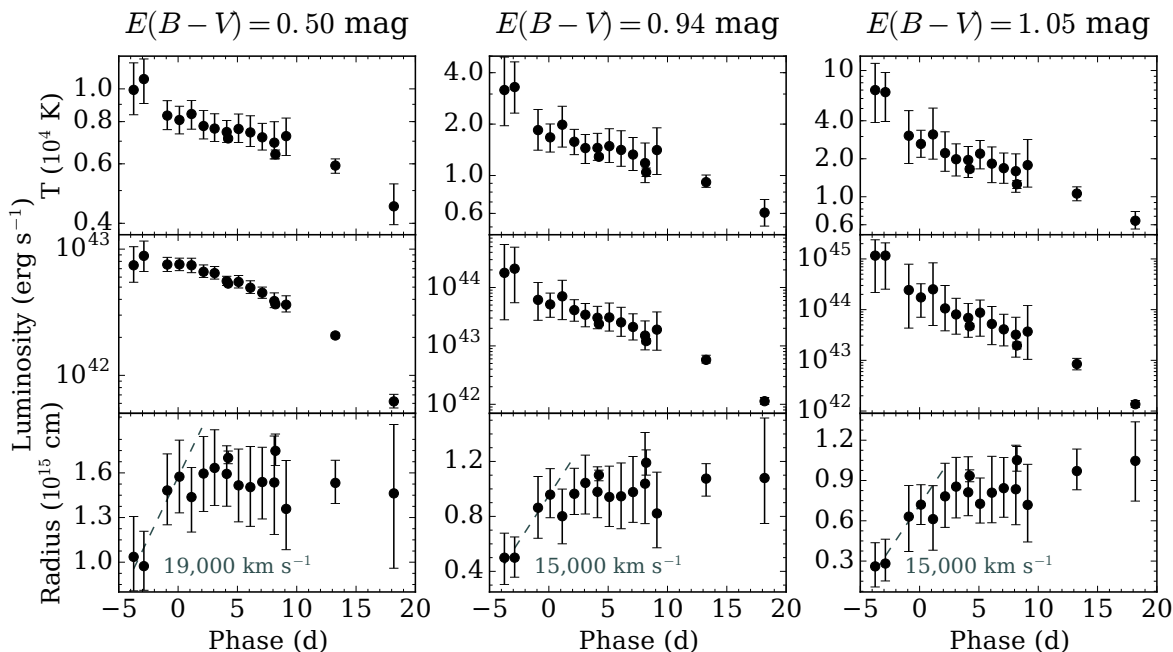


**Figure 14.** The best-fit blackbody temperature, bolometric luminosity, and radius evolution of SN 2015U for three assumed values of  $E(B-V)$  as a function of phase relative to V-band peak. The leftmost column shows the evolution assuming a value of 0.5 mag, the middle column assumes our preferred value of 0.94 mag, and the rightmost column corresponds to a value of 1.05 mag. In the lower panels, we show linear fits to the radius evolution up to V-band peak with a grey dashed line. All parameters are fitted using maximum-likelihood MCMC methods and error bars represent 95% confidence intervals (but do not include errors caused by uncertainty in the degree of host-galaxy dust reddening).

created by SN 2015U would require more sophisticated treatment, we place a rough upper limit on the value by assuming that the ejecta+CSM system of SN 2015U completely traps any radioactively produced  $\gamma$ -rays and that there is no luminosity contribution from ongoing interaction beyond our last detection at  $\sim 20$  days.

Our most constraining observation of a putative radioactively powered tail is a nondetection in the  $R$  band at +36 d. Our last multiband photometric measurement of the temperature yields  $T = 6000 \pm 1000$  K at +18 d (see §3.5). We adopt that temperature to calculate the blackbody luminosity for a source at our nondetection threshold, but we note that the temperature is still changing at this time, possibly affecting our results. This calculation yields an upper limit of  $M_{\text{Ni}} \lesssim 0.02 M_{\odot}$  — quite low for SNe I ( $M_{\text{Ni, Ia}} \gtrsim 0.4 M_{\odot}$ ,  $M_{\text{Ni, Ib/c}} \approx 0.2 M_{\odot}$ ; Contardo et al. 2000; Drout et al. 2011), but within the range of values observed for SNe II ( $M_{\text{Ni, II}} \approx 0.0016\text{--}0.26 M_{\odot}$ ; Hamuy 2003).

### 3.7 Progenitor Mass-Loss Rate

We adopt the simple shock-wind interaction model of Chevalier & Irwin (2011) to estimate the properties of the CSM surrounding SN 2015U. We assume that the CSM is spherically symmetric and follows a wind-like density profile ( $\rho \propto r^{-2}$ ), and we use the opacity of helium-dominated material in our calculations ( $\kappa = 0.2 \text{ cm}^2 \text{ g}^{-1}$ ). Margutti et al. (2014) solve the Chevalier & Irwin (2011) model in terms of three observables: break-out radius  $R_{\text{bo}}$  (the radius at which radiation diffuses forward ahead of the shock), total radiated energy  $E_{\text{rad}}$ , and light-curve rise time  $t_{\text{rise}}$ . We use  $t_{\text{rise}} = 9$  days and,

assuming  $E(B-V)_{\text{host}} = 0.94$  mag, we adopt  $E_{\text{rad}} = 7.1 \times 10^{49}$  erg from Table 4. For  $R_{\text{bo}}$  we take the first measured blackbody radius from Figure 14:  $R_{\text{bo}} = 5 \times 10^{14}$  cm. The resultant mass-loss estimate is very large,  $\dot{M} \approx 1.2 M_{\odot} \text{ yr}^{-1}$ . However, in this model  $\dot{M} \propto R_{\text{bo}}^{-3}$ , and there is reason to believe that our measurement of the blackbody radius before peak brightness does not reflect the true  $R_{\text{bo}}$  (see §3.5). If we instead use  $R_{\text{bo}} = 9 \times 10^{14}$  cm, the blackbody radius at V-band peak, we calculate  $\dot{M} \approx 0.2 M_{\odot} \text{ yr}^{-1}$ .

Both of these values are several orders of magnitude above the most extreme mass-loss rates produced by steady winds from stars, but they are not far from the time-averaged eruptive mass-loss rates from LBVs (which may well exhibit much higher instantaneous mass-loss rates; Smith 2014). Observations of iPTF13beo, a recent SN Ibn discovered by the intermediate Palomar Transient Factory (iPTF), implied an even higher (but short-lived) mass-loss rate of  $\dot{M} \approx 2.4 M_{\odot} \text{ yr}^{-1}$  immediately before the progenitor underwent core collapse (estimated via similar methods; Gorbikov et al. 2014).

If the CSM around SN 2015U was launched from the surface explosively rather than through a steady wind, the assumption that  $\rho_{\text{CSM}} \propto r^{-2}$  is suspect. In fact, the lack of an interaction-powered tail in the light curve of SN 2015U indicates that the density profile cannot be wind-like: Chevalier & Irwin (2011) show that ongoing interaction with a wind-like CSM powers a tail with  $L \propto t^{-0.6}$ , and SN 2015U fades more rapidly than that throughout its post-peak evolution. The lack of any high-velocity features in our spectra argues that this outer CSM must be optically thick at least out to the radius of the shock at the time of our last spec-

trum. Assuming  $v_{\text{shock}} \approx 20,000 \text{ km s}^{-1}$ , the velocity of the fastest material in unshrouded stripped-envelope SNe, this produces an estimate for the CSM extent of  $R \gtrsim 3 \times 10^{15} \text{ cm}$ . Adopting the average He I velocity measured from our spectra ( $745 \text{ km s}^{-1}$ ), material at that radius was launched 1–2 yr before core collapse. However, it is likely that the SN ejecta are slowed by its collision with the CSM, and so it may be more physically relevant to assume the CSM extent to be  $R \gtrsim 9 \times 10^{14} \text{ cm}$  (the blackbody radius at V-band peak); material at that radius was launched  $< 1 \text{ yr}$  before collapse.

It is not clear whether the extreme mass loss from SN 2015U’s progenitor was episodic and brief or sustained over a year or more, nor is it known whether the assumption of spherical symmetry is appropriate. We leave a more thorough examination of these questions to future work.

### 3.8 Constraints on Progenitor Variability

The presence of dense CSM suggests a recent history of extreme mass loss and perhaps variability of the progenitor star. SN Ibn 2006jc, for example, underwent a bright outburst ( $M = -14 \text{ mag}$ ) about 2 yr before becoming a genuine SN (Nakano et al. 2006; Foley et al. 2007; Pastorello et al. 2007), and there are multiple cases where SN IIn progenitors have been detected in outburst in the years prior to core collapse (e.g., Ofek et al. 2014), though such outbursts do not appear to be ubiquitous (e.g., Bilinski et al. 2015). KAIT has been monitoring NGC 2388 for almost 20 yr and we searched this extensive dataset for evidence of pre-explosion variability. We augment our unfiltered KAIT data with the publicly available PTF/iPTF images of the field in the  $r$  passband.<sup>10</sup>

Examining 758 images with observed upper limits fainter than 17.0 mag from 1998 Oct. through 2015 Feb. 10, we find no evidence for previous outbursts of the progenitor based upon difference imaging (using one of our deepest single exposures as a template). We stacked our images into rolling-window time bins 20 d wide and subtracted templates to search for evidence of previous outbursts of that timescale, but found none. We also stacked all images together and searched for evidence of a progenitor, but found none. (Note that we stacked the KAIT and PTF/iPTF images separately, and we did not perform difference imaging on these very deep stacks, as we had no templates with which to compare.) Figure 15 plots our  $1\sigma$  single-image nondetections and the observed light curve of SN 2015U.

Though we have regular imaging of NGC 2388 most years since 1998, the field was inaccessible to our telescopes for several months every year, so there are significant gaps, especially compared to the timescale of SN 2015U’s light curve ( $\sim 20 \text{ d}$ ). The orange bars along the bottom of Figure 15 mark every night at which more than 20 days had passed since the previous upper limit, indicating timespans when a previous SN 2015U-like event could have occurred undetected.

Unfortunately, even the epochs that were covered by our monitoring campaigns do not yield stringent constraints on the luminosity of a previous outburst, partially owing to the estimated  $\sim 1.5 \text{ mag}$  of host-galaxy dust extinction along the line of sight toward SN 2015U. The detected outburst

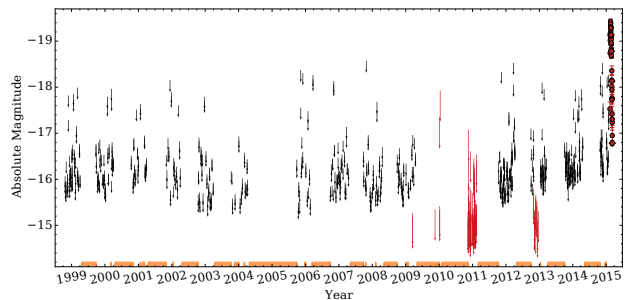


**Figure 15.** Our  $1\sigma$  nondetections from KAIT unfiltered images (black) and PTF/iPTF  $R$  images (red). The light curve of SN 2015U is shown to the far right. Timespans for which no upper limit had been obtained for at least 20 days are marked in orange along the bottom.

of SN 2006jc’s precursor reached a peak of  $M_r \approx -14.1 \text{ mag}$  (Pastorello et al. 2007), and such an outburst in SN 2015U’s precursor would have probably remained undetected by our monitoring campaign.

## 4 CONCLUSION

In this paper we presented observations of SN 2015U, a highly extinguished, low-velocity, rapidly evolving, luminous, apparently hydrogen-free SN which exploded in the strongly star-forming galaxy NGC 2388. Though detailed modeling has yet to be performed, and the degree of host-galaxy dust interference is uncertain, our data indicate that SN 2015U was a core-collapse SN with a peak powered by shock breakout from a dense CSM rather than radioactive decay. We suggest that this CSM was not wind-like but was instead created by at least one extreme episode of mass loss ( $\dot{M} \approx 0.2\text{--}1.2 M_{\odot} \text{ yr}^{-1}$ ) within a few years of core collapse. The CSM that surrounded SN 2015U was effectively hydrogen-free but was helium-rich; we also detect features from nitrogen, iron, and probably carbon in our spectra. No long-lasting light-curve tail was observed from radioactivity or from ongoing CSM interaction, implying that SN 2015U produced a relatively small amount of  $^{56}\text{Ni}$  compared to normal SNe Ib/c.

SN 2015U is a remarkably well-observed SN Ibn, especially among the rapidly fading subset of these events, and we find many similarities between it and other SNe in the literature. Modern surveys indicate the existence of a class of blue, continuum-dominated, hydrogen-deficient, luminous, and rapidly evolving SNe including those found by Drout et al. (2014) and Arcavi et al. (2016); our analysis of SN 2015U implies fundamental similarities between these events, a subset of the SNe Ibn (e.g., Pastorello et al. 2016), and other rapidly fading SNe of lower luminosity (i.e., SN 2002bj and SN 2010X). While the exact progenitors of these events are quite uncertain, it is clear that they demand extreme mass-loss rates from their stripped-envelope progenitor stars.

<sup>10</sup> <http://irsa.ipac.caltech.edu/applications/ptf/>

## ACKNOWLEDGEMENTS

The authors thank M. Drout, R. Foley, P. Nugent, D. Kasen, E. Quataert, D. Poznanski, and O. Fox for useful comments and discussions. We are grateful to our referee, A. Pastorello, for comments that have greatly improved this effort. We thank the *HST*, Keck Observatory, and Lick Observatory staffs for their expert assistance with the observations. We also acknowledge the following Nickel 1 m observers and KAIT checkers for their valuable assistance with this work: A. Bigley, C. Gould, G. Halevi, K. Hayakawa, A. Hughes, H.J. Kim, M. Kim, P. Lu, K. Pina, T. Ross, S. Stegman, and H. Yuk.

A.V.F.'s supernova research group at U. C. Berkeley is supported by NSF grant AST-1211916, the TABASGO Foundation, Gary and Cynthia Bengier, and the Christopher R. Redlich Fund. Additional assistance is provided by NASA/*HST* grants AR-14295 and GO-14149 from the Space Telescope Science Institute, which is operated by the Association of Universities for Research in Astronomy, Inc., under NASA contract NAS5-26555. J.M.S. is supported by an NSF Astronomy and Astrophysics Postdoctoral Fellowship under award AST-1302771.

Some of the data presented herein were obtained at the W. M. Keck Observatory, which is operated as a scientific partnership among the California Institute of Technology, the University of California, and NASA; the observatory was made possible by the generous financial support of the W. M. Keck Foundation.

KAIT and its ongoing operation were supported by donations from Sun Microsystems, Inc., the Hewlett-Packard Company, AutoScope Corporation, Lick Observatory, the NSF, the University of California, the Sylvia and Jim Katzman Foundation, and the TABASGO Foundation. Research at Lick Observatory is partially supported by a very generous gift from Google, as well as by contributions from numerous individuals including Eliza Brown and Hal Candee, Kathy Burck and Gilbert Montoya, David and Linda Cornfield, William and Phyllis Draper, Luke Ellis and Laura Sawczuk, Alan and Gladys Hoefer, DuBose and Nancy Montgomery, Jeanne and Sanford Robertson, Stanley and Miriam Schiffman, Thomas and Alison Schneider, the Hugh Stuart Center Charitable Trust, Mary-Lou Smulders and Nicholas Hodson, Clark and Sharon Winslow, Weldon and Ruth Wood, and many others.

This research was based in part on data taken with the NASA/ESA *Hubble Space Telescope*, and obtained from the Hubble Legacy Archive, which is a collaboration between the Space Telescope Science Institute (STScI/NASA), the Space Telescope European Coordinating Facility (ST-ECF/ESA), and the Canadian Astronomy Data Centre (CADC/NRC/CSA). We also made use of the NASA/IPAC Extragalactic Database (NED) which is operated by the Jet Propulsion Laboratory, California Institute of Technology, under contract with NASA.

## REFERENCES

Anderson J. P., et al., 2014, *ApJ*, **786**, 67  
 Anupama G. C., Sivarani T., Pandey G., 2001, *A&A*, **367**, 506  
 Arcavi I., et al., 2012, *ApJ*, **756**, L30  
 Arcavi I., et al., 2016, *ApJ*, **819**, 35

Arnett W. D., 1982, *ApJ*, **253**, 785  
 Auer L. H., van Blerkom D., 1972, *ApJ*, **178**, 175  
 Baron D., Poznanski D., Watson D., Yao Y., Prochaska J. X., 2015, *MNRAS*, **447**, 545  
 Bianco F. B., et al., 2014, *ApJS*, **213**, 19  
 Bilinski C., Smith N., Li W., Williams G. G., Zheng W., Filippenko A. V., 2015, *MNRAS*, **450**, 246  
 Brocklehurst M., 1971, *MNRAS*, **153**, 471  
 Cardelli J. A., Clayton G. C., Mathis J. S., 1989, *ApJ*, **345**, 245  
 Chevalier R. A., Irwin C. M., 2011, *ApJ*, **729**, L6  
 Choi J., Dotter A., Conroy C., Cantiello M., Paxton B., Johnson B. D., 2016, *ApJ*, **823**, 102  
 Chugai N. N., 2001, *MNRAS*, **326**, 1448  
 Chugai N. N., et al., 2004, *MNRAS*, **352**, 1213  
 Clayton G. C., Mathis J. S., 1988, *ApJ*, **327**, 911  
 Contardo G., Leibundgut B., Vacca W. D., 2000, *A&A*, **359**, 876  
 Coyne G. V., Gehrels T., 1966, *AJ*, **71**, 355  
 Dessart L., Hillier D. J., Livne E., Yoon S.-C., Woosley S., Waldman R., Langer N., 2011, *MNRAS*, **414**, 2985  
 Dessart L., Hillier D. J., Woosley S., Livne E., Waldman R., Yoon S.-C., Langer N., 2015, *MNRAS*, **453**, 2189  
 Drout M. R., et al., 2011, *ApJ*, **741**, 97  
 Drout M. R., et al., 2013, *ApJ*, **774**, 58  
 Drout M. R., et al., 2014, *ApJ*, **794**, 23  
 Eastman R. G., Schmidt B. P., Kirshner R., 1996, *ApJ*, **466**, 911  
 Faber S. M., et al., 2003, in Iye M., Moorwood A. F. M., eds, *Society of Photo-Optical Instrumentation Engineers (SPIE) Conference Series Vol. 4841, Instrument Design and Performance for Optical/Infrared Ground-based Telescopes*. pp 1657–1669, doi:10.1117/12.460346  
 Fassia A., et al., 2000, *MNRAS*, **318**, 1093  
 Fassia A., et al., 2001, *MNRAS*, **325**, 907  
 Filippenko A. V., 1982, *PASP*, **94**, 715  
 Filippenko A. V., 1991, in Danziger I. J., Kjaer K., eds, *European Southern Observatory Conference and Workshop Proceedings Vol. 37, European Southern Observatory Conference and Workshop Proceedings*. p. 343  
 Filippenko A. V., 1997, *ARA&A*, **35**, 309  
 Filippenko A. V., Li W. D., Treffers R. R., Modjaz M., 2001, in Paczynski B., Chen W.-P., Lemme C., eds, *Astronomical Society of the Pacific Conference Series Vol. 246, IAU Colloq. 183: Small Telescope Astronomy on Global Scales*. p. 121  
 Foley R. J., Smith N., Ganeshalingam M., Li W., Chornock R., Filippenko A. V., 2007, *ApJ*, **657**, L105  
 Fransson C., et al., 2014, *ApJ*, **797**, 118  
 Friedman S. D., et al., 2011, *ApJ*, **727**, 33  
 Gal-Yam A., 2012, *Science*, **337**, 927  
 Gal-Yam A., et al., 2014, *Nature*, **509**, 471  
 Ganeshalingam M., et al., 2010, *ApJS*, **190**, 418  
 Gehrels T., Silvester A. B., 1965, *AJ*, **70**, 579  
 Gorbikov E., et al., 2014, *MNRAS*, **443**, 671  
 Hamuy M., 2003, *ApJ*, **582**, 905  
 Herbig G. H., 1995, *ARA&A*, **33**, 19  
 Hershkowitz S., Linder E., Wagoner R. V., 1986, *ApJ*, **301**, 220  
 Hillier D. J., 1991, *A&A*, **247**, 455  
 Kankare E., et al., 2012, *MNRAS*, **424**, 855  
 Kasen D., Woosley S. E., 2009, *ApJ*, **703**, 2205  
 Kasliwal M. M., et al., 2010, *ApJ*, **723**, L98  
 Khazov D., et al., 2016, *ApJ*, **818**, 3  
 Kleiser I. K. W., Kasen D., 2014, *MNRAS*, **438**, 318  
 Kumar S., Yuk H., Zheng W., Filippenko A. V., 2015, *Central Bureau Electronic Telegrams*, 4164, 1  
 Lan T.-W., Ménard B., Zhu G., 2015, *MNRAS*, **452**, 3629  
 Leonard D. C., Filippenko A. V., Barth A. J., Matheson T., 2000, *ApJ*, **536**, 239  
 Li W., Filippenko A. V., Chornock R., Jha S., 2003, *PASP*, **115**, 844

Liu Y.-Q., Modjaz M., Bianco F. B., Graur O., 2015, preprint, ([arXiv:1510.08049](https://arxiv.org/abs/1510.08049))

Margutti R., et al., 2014, *ApJ*, **780**, 21

Matheson T., 2001, *PASP*, **113**, 1155

Matheson T., et al., 2000, *AJ*, **120**, 1487

Matheson T., Filippenko A. V., Li W., Leonard D. C., Shields J. C., 2001, *AJ*, **121**, 1648

Mattila S., et al., 2008, *MNRAS*, **389**, 141

Mauerhan J. C., et al., 2013, *MNRAS*, **431**, 2599

Mauerhan J. C., et al., 2015, *MNRAS*, **453**, 4467

Milisavljevic D., et al., 2015, *ApJ*, **815**, 120

Miller J., Stone R., 1993, Lick Observatory Technical Reports, 66

Modjaz M., et al., 2014, *AJ*, **147**, 99

Moriya T., Tominaga N., Blinnikov S. I., Baklanov P. V., Sorokina E. I., 2011, *MNRAS*, **415**, 199

Nachman P., Hobbs L. M., 1973, *ApJ*, **182**, 481

Nakano S., Itagaki K., Puckett T., Gorelli R., 2006, Central Bureau Electronic Telegrams, **666**, 1

Ochner P., et al., 2015, The Astronomer's Telegram, **7105**, 1

Ofek E. O., et al., 2010, *ApJ*, **724**, 1396

Ofek E. O., et al., 2014, *ApJ*, **789**, 104

Pastorello A., et al., 2007, *Nature*, **447**, 829

Pastorello A., et al., 2008a, *MNRAS*, **389**, 113

Pastorello A., et al., 2008b, *MNRAS*, **389**, 131

Pastorello A., et al., 2015a, *MNRAS*, **449**, 1921

Pastorello A., et al., 2015b, *MNRAS*, **449**, 1954

Pastorello A., et al., 2015c, *MNRAS*, **454**, 4293

Pastorello A., et al., 2016, *MNRAS*, **456**, 853

Patat F., et al., 2007, *Science*, **317**, 924

Patat F., et al., 2015, *A&A*, **577**, A53

Pereira-Santaella M., et al., 2015, *A&A*, **577**, A78

Pérez F., Granger B. E., 2007, *Computing in Science and Engineering*, **9**, 21

Phillips M. M., et al., 2013, *ApJ*, **779**, 38

Popov D. V., 1993, *ApJ*, **414**, 712

Poznanski D., et al., 2010, *Science*, **327**, 58

Poznanski D., Prochaska J. X., Bloom J. S., 2012, *MNRAS*, **426**, 1465

Rabinak I., Waxman E., 2011, *ApJ*, **728**, 63

Riess A. G., et al., 1999, *AJ*, **118**, 2675

Sanders N. E., et al., 2015, *ApJ*, **799**, 208

Schlafly E. F., Finkbeiner D. P., 2011, *ApJ*, **737**, 103

Schlegel E. M., 1990, *MNRAS*, **244**, 269

Serkowski K., Mathewson D. S., Ford V. L., 1975, *ApJ*, **196**, 261

Shivvers I., Groh J. H., Mauerhan J. C., Fox O. D., Leonard D. C., Filippenko A. V., 2015, *ApJ*, **806**, 213

Silverman J. M., Kleiser I. K. W., Morton A. J. L., Filippenko A. V., 2010, Central Bureau Electronic Telegrams, **2223**

Silverman J. M., et al., 2012, *MNRAS*, **425**, 1789

Silverman J. M., et al., 2013a, *ApJS*, **207**, 3

Silverman J. M., et al., 2013b, *ApJ*, **772**, 125

Smith N., 2014, *ARA&A*, **52**, 487

Smith N., Foley R. J., Filippenko A. V., 2008, *ApJ*, **680**, 568

Somerville W. B., 1988, *The Observatory*, **108**, 44

Stetson P. B., 1987, *PASP*, **99**, 191

Strömgren B., 1948, *ApJ*, **108**, 242

Tsvetkov D. Y., Volkov I. M., Pavlyuk N. N., 2015, *Information Bulletin on Variable Stars*, **6140**, 1

Wheeler J. C., Johnson V., Clocchiatti A., 2015, *MNRAS*, **450**, 1295

Whittet D. C. B., Martin P. G., Hough J. H., Rouse M. F., Bailey J. A., Axon D. J., 1992, *ApJ*, **386**, 562

Wright E. L., 2006, *PASP*, **118**, 1711

Yaron O., Gal-Yam A., 2012, *PASP*, **124**, 668

de Vaucouleurs G., de Vaucouleurs A., Corwin Jr. H. G., Buta R. J., Paturel G., Fouqué P., 1991, *Third Reference Catalogue of Bright Galaxies. Volume I: Explanations and references.*

Volume II: Data for galaxies between  $0^h$  and  $12^h$ . Volume III: Data for galaxies between  $12^h$  and  $24^h$ .

This paper has been typeset from a  $\text{\TeX}/\text{\LaTeX}$  file prepared by the author.